

First onset of unrest captured geodetically at Socompa Volcano, Northern Chile

Fei Liu¹, John Ross Elliott¹, Susanna K Ebmeier¹, Timothy James Craig¹, Andrew Hooper¹, Camila Novoa Lizama¹, and Francisco Delgado²

¹University of Leeds

²Institut de Physique du Globe de Paris

January 3, 2023

Abstract

We report the first detection of unrest at Socompa, Northern Chile, a stratovolcano which has recorded no eruptions since ~7,200 years ago. We measure deformation at and around Socompa using Interferometric Synthetic Aperture Radar (InSAR) observations between Jan 2018 and Oct 2021. We find that, whilst initially inactive, Socompa shows a steady uplift (17.5 mm/yr) from Dec 2019, independently recorded by near-field continuous Global Positioning System (GPS) data. The data can be fit with pressure increase in an ellipsoidal source region stretching from 1.9 to 9.5 km, with a volume change rate of $\sim 5.8 \times 10^6$ m³/yr. Our observations of the onset of uplift preclude the possibility that a nearby Mw 6.8 deep intraslab earthquake on 3rd June 2020 triggered the unrest. The deformation signal we detect indicates the initiation of unrest at Socompa, after at least two decades without measurable deformation, and many thousands of years without volcanic activity.

Hosted file

951758_0_art_file_10518701_rmldxy.docx available at <https://authorea.com/users/565251/articles/612257-first-onset-of-unrest-captured-geodetically-at-socompa-volcano-northern-chile>

1 **First onset of unrest captured geodetically at Socompa Volcano, Northern Chile**

2 **F. Liu¹, J. R. Elliott¹, S. K. Ebmeier¹, T. J. Craig¹, A. Hooper¹,**

3 **C. Novoa Lizama¹, and F. Delgado²**

4 ¹COMET, School of Earth and Environment, University of Leeds, Leeds, United Kingdom

5 ²Department of Geology and Centro de Excelencia en Geotermia Andina, Universidad de

6 Chile, Santiago, Chile

7 Corresponding author: Fei Liu (eefl@leeds.ac.uk)

8 **Key Points:**

- 9 • InSAR and GPS observations show the first detection of unrest at Socompa volcano
10 with steady uplift up to 17.5 mm/yr since Dec 2019.
- 11 • Deformation patterns are consistent with an ellipsoidal source, stretching from 1.9 to
12 9.5 km and with a volume change of $\sim 5.8 \times 10^6 \text{ m}^3/\text{yr}$.
- 13 • We combine InSAR and GPS to find the onset time of Socompa uplift, which has not
14 previously been possible at a Central Andean volcano.

15 **Abstract**

16 We report the first detection of unrest at Socompa, Northern Chile, a stratovolcano which has
17 recorded no eruptions since ~7,200 years ago. We measure deformation at and around
18 Socompa using Interferometric Synthetic Aperture Radar (InSAR) observations between Jan
19 2018 and Oct 2021. We find that, whilst initially inactive, Socompa shows a steady uplift
20 (17.5 mm/yr) from Dec 2019, independently recorded by near-field continuous Global
21 Positioning System (GPS) data. The data can be fit with pressure increase in an ellipsoidal
22 source region stretching from 1.9 to 9.5 km, with a volume change rate of $\sim 5.8 \times 10^6 \text{ m}^3/\text{yr}$.
23 Our observations of the onset of uplift preclude the possibility that a nearby M_w 6.8 deep
24 intraslab earthquake on 3rd June 2020 triggered the unrest. The deformation signal we detect
25 indicates the initiation of unrest at Socompa, after at least two decades without measurable
26 deformation, and many thousands of years without volcanic activity.

27 **Plain Language Summary**

28 Here we report the first observation of unrest of the Socompa volcano, Northern Chile, which
29 is thought to have last erupted thousands of years ago. Using an established remote sensing
30 technique called radar interferometry and differencing radar images from two dates, it is
31 possible to retrieve millimetre-level surface displacements during this period. Here, we use a
32 time series of multiple images spanning Jan 2018 to Oct 2021, over the Atacama region in
33 Northern Chile, to estimate the change in ground movement through time. Combined with
34 GPS data, we find Socompa volcano started to uplift in Dec 2019 at a relatively stable speed
35 (of 17.5 mm/yr) without any trace of slowing down up to Dec 2021. Our analysis excludes
36 the possibility that this volcanic deformation is triggered by a nearby 112 km depth, M_w 6.8
37 earthquake, which occurred in June 2020, thus after the onset time. Deformation at Socompa
38 has similarities with other volcanoes in the Central Andes, where low rates of magmatic
39 uplift have been detected at other apparently quiescent volcanoes. Such large-scale

40 monitoring efforts using remote sensing data are important, as we can better understand the
41 deformation style of these volcanoes in areas that are poorly instrumented.

42 **1 Introduction**

43 Interferometric Synthetic Aperture Radar (InSAR) permits measurement of the
44 Earth's surface deformation at the millimetre-level, transforming our understanding of
45 volcanic deformation and magma movement through increasing the number of volcanoes
46 where deformation has been studied by an order of magnitude (e.g., Biggs et al., 2014;
47 Ebmeier et al., 2018; Poland & Zebker, 2022). InSAR can capture deformation caused by the
48 movement of magma through the Earth's crust (e.g., Reath et al., 2019), by pressure changes
49 within a zone of magma storage (e.g., Chaussard & Amelung, 2012) or overlying
50 hydrothermal system (e.g., Yunjun et al., 2021). In Northern Chile (17.5-27°S), where only
51 10 of the region's 42 Holocene volcanoes are currently actively monitored using ground-
52 based instrumentation (Aguilera et al., 2022), the systematic displacement measurements
53 possible with InSAR can provide the best record of timings of recent unrest and magmatic
54 activity at Central Andean volcanoes (e.g., Pritchard & Simons, 2004a; Henderson &
55 Pritchard, 2013; MacQueen et al., 2020).

56 Survey-mode InSAR first detected magmatic deformation in the Central Andes at
57 Uturuncu, Lazufre, Cerro Blanco and Sabanacaya-Hualca Hualca in ~1990s (Pritchard &
58 Simons, 2002). Uturuncu has been the subject of numerous subsequent studies (e.g., Fialko &
59 Pearse, 2012; Hickey et al., 2013; Henderson & Pritchard, 2013; Henderson & Pritchard,
60 2017; Barone et al., 2019), showing the reservoir depth of 15-30 km and is potentially related
61 to deeper magma movement associated with the Altiplano-Puna Magma Body (APMB, Ward
62 et al., 2014). The deformation signal near Cerro Overo, which has no ground-based
63 monitoring, transitioned from subsidence to uplift in ~2003-2005, which involves fluid
64 accumulation and loss within the crust at ~10 km depth (Henderson & Pritchard, 2013). The

65 deformation pattern of uplift at Lazufre (Lastarria and Azufre) has been interpreted to
66 represent magma accumulation in the mid-upper crust with source depth < 10 km (Ruch &
67 Walter, 2010; Pearse & Lundgren, 2013; Remy et al., 2014; Díaz et al., 2015; Henderson et
68 al., 2017). Other deformation, for example during the 2010 unrest at Lascar (which erupted in
69 2015-2017, without deformation, Gaete et al., 2020) can be linked to crater evolution
70 processes such as gravitational slumping or piston-like subsidence (Richter et al., 2018).
71 Putana showed a short-lived low magnitude uplift in 2009 related to hydrothermal activity
72 (Henderson & Pritchard, 2013; Stebel et al., 2014).

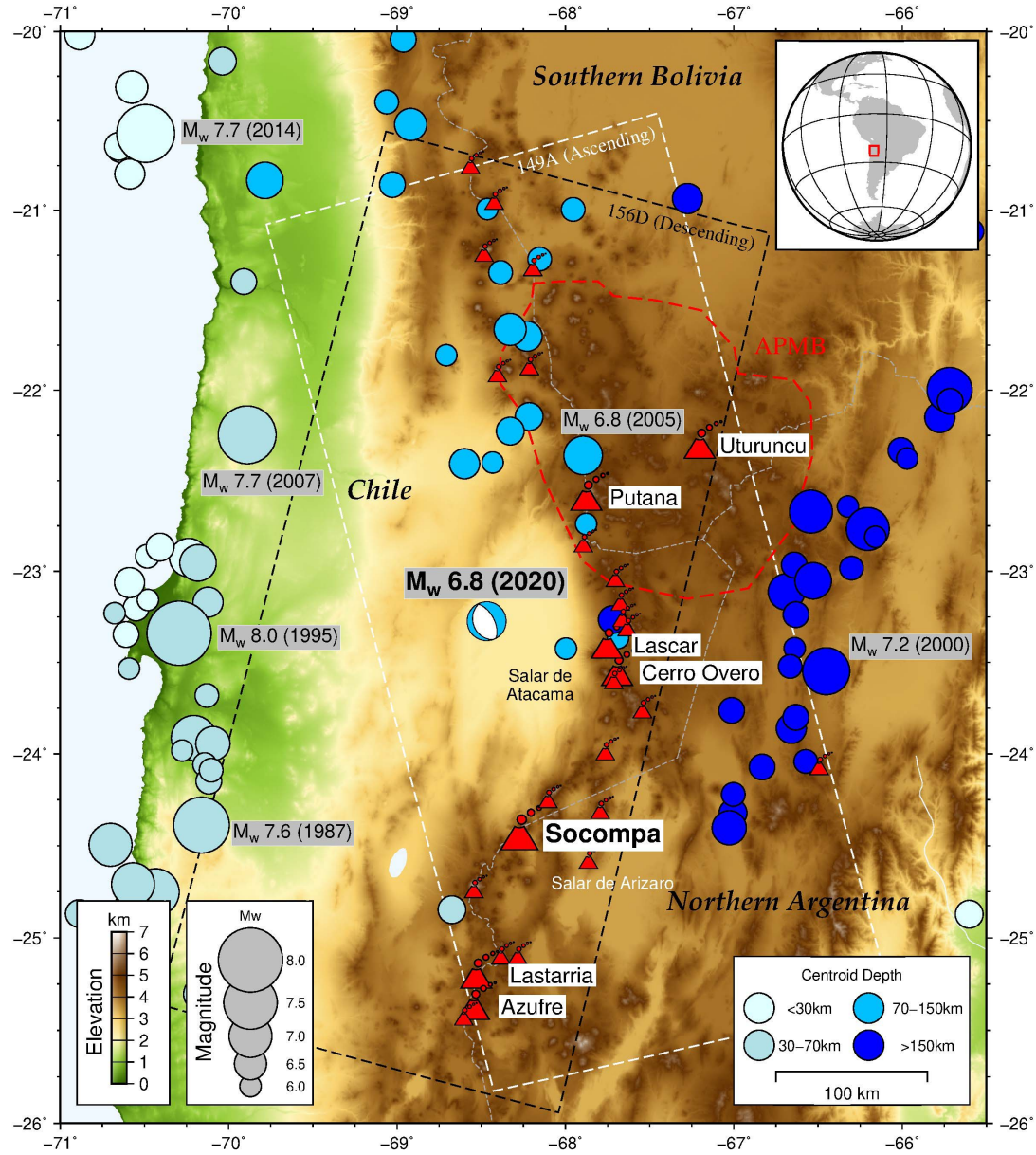
73 The triggers for episodes of magmatic uplift (or subsidence) in the Central Andes are
74 obscure but could potentially include (1) variations in flux from lower crustal bodies of melt
75 (e.g., the APMB) or (2) changes within shallow reservoirs such as crystallisation or degassing
76 as inferred in other settings (Pritchard et al., 2019). These processes cause pressure changes
77 within reservoirs, thus controlling the initiation and cessation of inflation (or deflation). The
78 initiation of deformation may be linked to external events like earthquakes. For example,
79 large subduction earthquakes in the Southern Andes and Japan caused stress field changes
80 that triggered episodes of subsidence at multiple volcanoes (Pritchard et al., 2013; Takada &
81 Fukushima, 2013), and regional earthquakes are also thought to have triggered delayed uplift
82 through surface waves (e.g., Lupi et al., 2017).

83 Here, we analyse ~4 years of Sentinel-1 InSAR time series data, spanning Jan 2018 to
84 Oct 2021, in the region of Antofagasta, Chile (Figure 1). Similarly to those previously
85 reported, we observe uplift at Uturuncu, and Cerro Overo and Azufre. However, we also find
86 a previously unreported deformation signal centred on the Socompa volcano, where no
87 deformation has previously been observed from regional InSAR studies (1992-2010,
88 Henderson & Pritchard, 2013). We measure a steady linear uplift (rate of 17.5 ± 3.7 mm/yr)

89 starting from Dec 2019, which continues through the rest of our InSAR observation time
90 (until Oct 2021).

91 Socompa is a large stratovolcano (peak elevation 6,031 m) and is the site of a trainline
92 and manned border control between Chile and Argentina. It is known for the failure of the
93 northwestern flank that produced a 600 km² debris-avalanche deposit and triggered post-
94 collapse eruptions ~7, 200 years ago (Wadge et al., 1995). As a result of its remote location
95 and presumed quiescence, it lacks targeted monitoring, although it was selected as the site of
96 a single Global Positioning System (GPS) station (SOCM) installed in 2011 as part of the
97 NSF PLUTONS network (Pritchard et al., 2018) due to its location halfway between Lazufre
98 and Uturuncu. A small lake at the foot, and several warmspots near the summit of the volcano
99 form a complex microbial ecosystem (Halloy, 1991; Costello et al., 2009; Farías et al., 2013)
100 where both water and CO₂ degassing have been observed during field studies (but not from a
101 satellite IR survey, Jay et al., 2013), implying the presence of active hydrothermal and
102 therefore magmatic systems.

103 We determine the precise onset time of Socompa uplift using a time-dependent
104 parameterized model fitting of the GPS time series from SOCM, and investigate the temporal
105 relationship between the onset of Socompa uplift and nearby earthquakes to explore the
106 potential trigger mechanisms. We reconstruct the cumulative deformation fields using an
107 InSAR time series approach (Liu et al., 2021), and combine both InSAR and GPS data as
108 inputs to assess several potential geodetic source models to explain the Socompa deformation.
109 Finally, we discuss the sudden onset of uplift at Socompa in the context of the long
110 timescales of unrest as observed with InSAR in the Central Andean volcanoes since the
111 1990s.



112

113 **Figure 1.** Topographic map of Northern Chile from SRTM. White and black dashed rectangle boxes show the
 114 Sentinel-1 data coverage from two tracks (149A Ascending and 156D Descending, spanning Jan 2018
 115 to Oct 2021). All Holocene volcanoes are marked and some active volcanoes with larger icons are labelled by
 116 their name. The red dashed line roughly defines the extent of the APMB (Perkins et al., 2016). The M_w 6.8
 117 earthquake epicentre (3rd Jun 2020 with a 112 km centroid depth), is marked by the focal mechanism, while all
 118 the $M_w > 6.0$ historical earthquakes since 1976 (where a precise global seismic network was established) in this
 119 region are shown by blue circles coloured by centroid depth (records from the United States Geological Survey,
 120 USGS).

121 **2 InSAR Time Series Analysis**

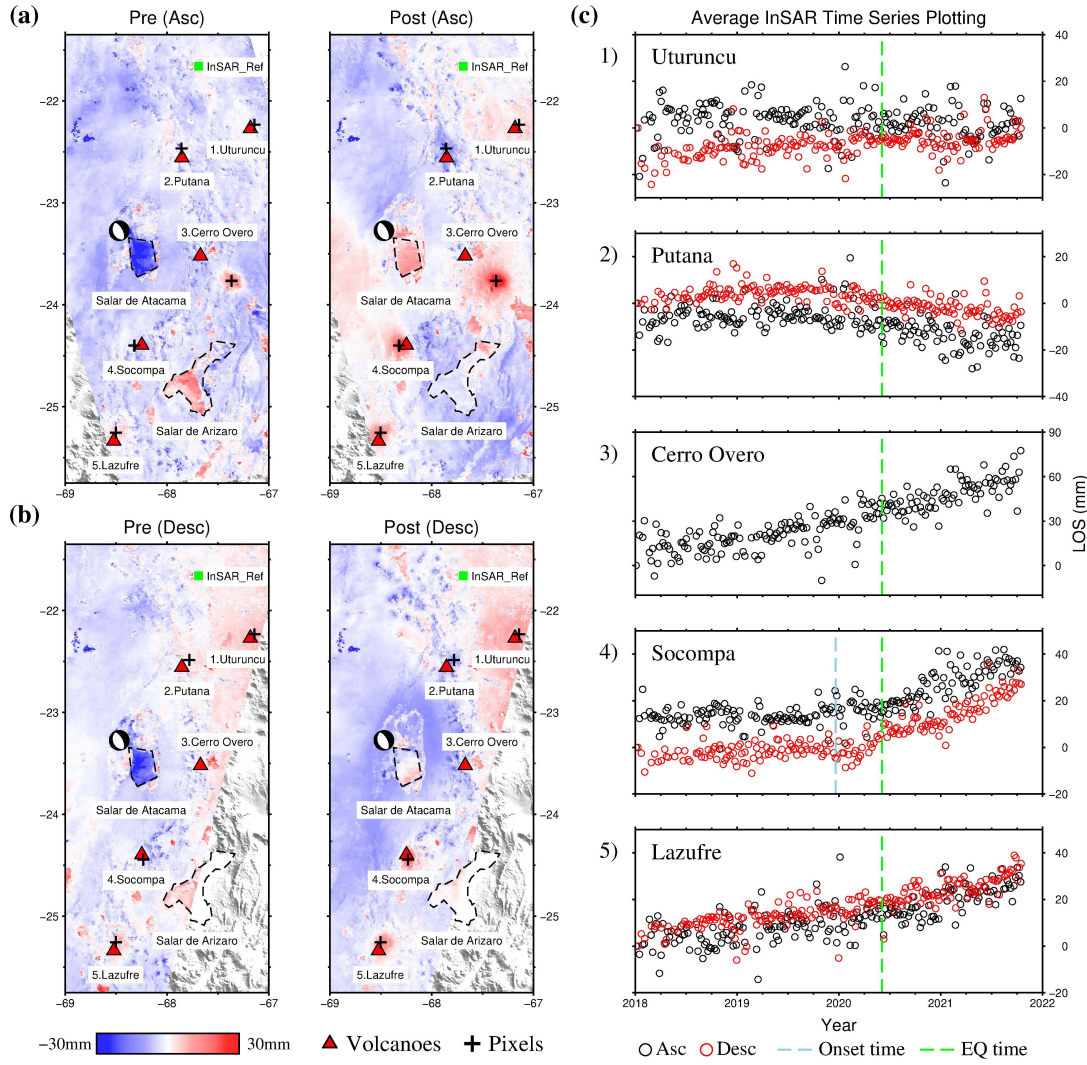
122 Here we process Sentinel-1 InSAR time series using LiCSAR processing chain
123 (Lazecky et al., 2020) and StaMPS software (Hooper et al., 2007, processing details in Text
124 S1). Compared to single interferograms, InSAR time series analysis provides frequent
125 estimates of surface displacement through time (every 6 or 12 days for Sentinel-1), reducing
126 measurement uncertainties from noise (Osmanoglu et al., 2016). In addition, if we assume a
127 deformation model appropriate for displacements due to Socoma unrest, we can reconstruct
128 the post-onset cumulative deformation field via a time-dependent parameterized model fitted
129 to the InSAR time series. As the observed velocity change at Socoma is approximately
130 linear, we assume that surface displacement at time t following the onset time t_0 can be
131 decomposed as follows:

132
$$\psi(t) = V_1 t + H(t - t_0)V_2 t + b \#(1)$$

133 where $H(*)$ is a Heaviside step function, V_1 is the background long-term linear deformation
134 rate, V_2 is the linear velocity change after the onset time, and b is a constant reference offset
135 in observations. We do not fit the seasonal signals because the already-applied GACOS
136 correction should suppress the seasonality, and it is also difficult to model it accurately
137 considering the noise level within the InSAR data in this region. After fitting the data, we
138 reconstruct the cumulative pre- and post-onset deformation field in the line of sight (LOS)
139 direction via the difference between the points at both ends of the fitting lines (Figure 2).

140 As the Central Andes predominately lacks vegetation, coherence is very high,
141 significantly lowering the impact of unwrapping errors and fading signals (Agram & Simons,
142 2015). The main InSAR error sources arise from atmospheric noise, including both
143 tropospheric and ionospheric components. Although the applied GACOS corrections (Yu et
144 al., 2018) improve the data quality (with average standard error reductions of 16.9% and 45.7%
145 for ascending and descending interferograms, respectively, Figure S1), the ionospheric noise

146 is very strong and could not be ignored, especially on ascending track. We therefore remove a
 147 linear ramp that spans the whole interferogram to reduce ionospheric noise, and other long
 148 wavelength signals associated with orbit errors and plate motion. Overall, the noise level in
 149 the ascending data is much higher than for descending, and noticeable atmospheric artefacts
 150 remain in high topography areas.



151
 152 **Figure 2.** Reconstructed pre- and post-onset cumulative deformation fields and corresponding InSAR time
 153 series plots. (a) The pre- and post-onset cumulative deformation fields using ascending track data. The focal
 154 mechanism, black dashed polygon, and green square represent the epicentre of the M_w 6.8 earthquake, the
 155 approximate boundaries of the salar (salt pan) regions, and the InSAR reference points, respectively. The InSAR

156 time series plots of some peak displacement pixels near the volcanoes are shown in (c). (b) Same as (a) but for
157 descending track data. In all figures, positive values mean movement towards the satellite. Note the
158 displacement signal associated with Cerro Overo is ~40 km southeast of the volcano and falls outside of the
159 data coverage on the descending frame.

160

161 **3 Socompa Uplift**

162 3.1 Onset Time determination

163 Determining the onset time for Socompa uplift is important not only for
164 reconstructing the cumulative deformation field, but also for investigating potential causes for
165 initiating unrest at Socompa. Due to historically lower temporal resolution satellite imagery
166 and the typically long duration of unrest, it has not previously been possible to precisely
167 determine the initiation time of deformation at a Central Andean volcano. For example, while
168 uplift at Sabancaya is known to have started in 2013, the distribution of SAR acquisitions
169 means that it could have taken place at any point over several months (Macqueen et al., 2020).

170 Here we investigate potential triggering mechanisms from earthquakes in this region by
171 exploring all major historical events ($M_w > 6.0$ since 1976, see Figure 1). We find the closest
172 event in space and time is a M_w 6.8 intraslab earthquake with a 112 km centroid depth, which
173 occurred on 3rd Jun 2020, and whose epicentre is ~120 km northwest of Socompa (Figure S2).
174 Initial visual inspection of the deformation signal pointed to the potential for a causal
175 relationship given the close correlation in time, but the InSAR time series are noisy and
176 contain seasonal signals that overprint changes in long-term trends.

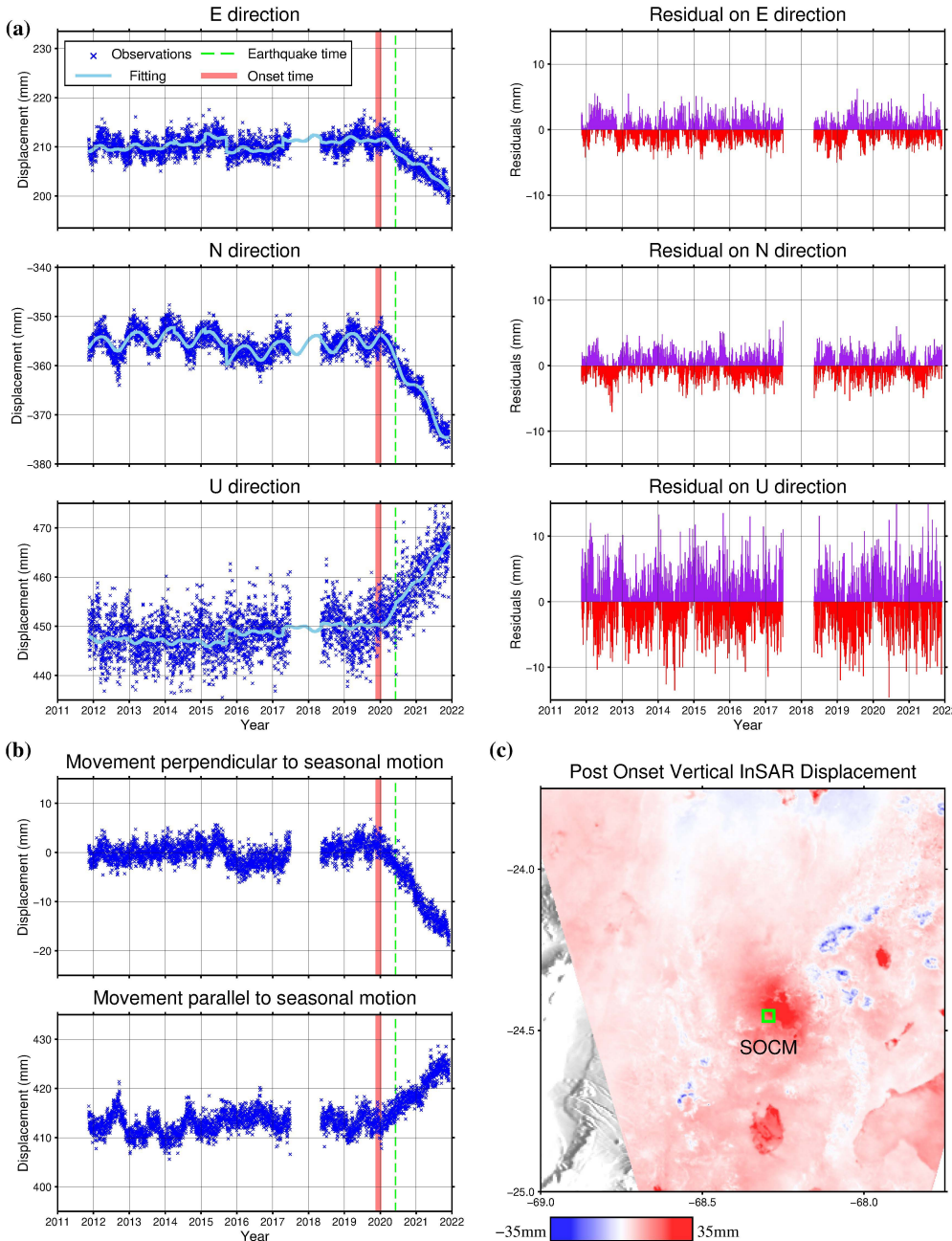
177 To determine the exact onset time, we collect data from a previously installed GPS
178 station (SOCM, Henderson et al., 2017), which is located ~8 km southwest of the Socompa
179 volcano and captures the deformation signal (Figure 3c). We use a time series with average
180 daily positions processed by the Nevada Geodetic Laboratory in a South American Plate

181 reference frame (Blewitt et al., 2018) to do a time-dependent parameterized fitting, using the
182 trajectory model:

$$183 \quad \delta(t) = V_1 t + H(t - t_0)V_2 t + A_1 \sin(2\pi t + \varphi_1) \\ + A_2 \sin(4\pi t + \varphi_2) + \sum H(t - t_{eq(i)})C_i + b \#(2)$$

184 where the unit of time t is year, A_1 , A_2 and φ_1 , φ_2 are the amplitudes and phases of annual
185 and semi-annual terms respectively, $t_{eq(i)}$ and C_i are historical earthquake event times and
186 corresponding coseismic offsets that are close to the station (based on the database of the
187 Nevada Geodetic Laboratory). We use a Markov Chain Monte Carlo approach to determine
188 that the optimal onset time t_0 is 14th Dec 2019 (173 ± 24 days ahead of the earthquake event
189 time), using all three components of GPS time series data and weighting them by the noise
190 level within each component (Figure 3a).

191 Such analysis highlights strong seasonal effects in the GPS time series, especially in
192 the North direction, leaving some uncertainty about the onset time in the data fitting. To
193 reduce the influence of seasonal signals, we further use a novel method of vector
194 decomposition, transforming the East-North vectors into another orthogonal coordinate
195 system, aligned along the movements parallel and perpendicular to the direction of seasonal
196 motion (Text S2). The decomposition results (Figure 3b) clearly show an onset time half a
197 year ahead of the earthquake, ruling out the possibility that unrest at Socompa was
198 dynamically triggered by seismic waves induced by this earthquake.



199

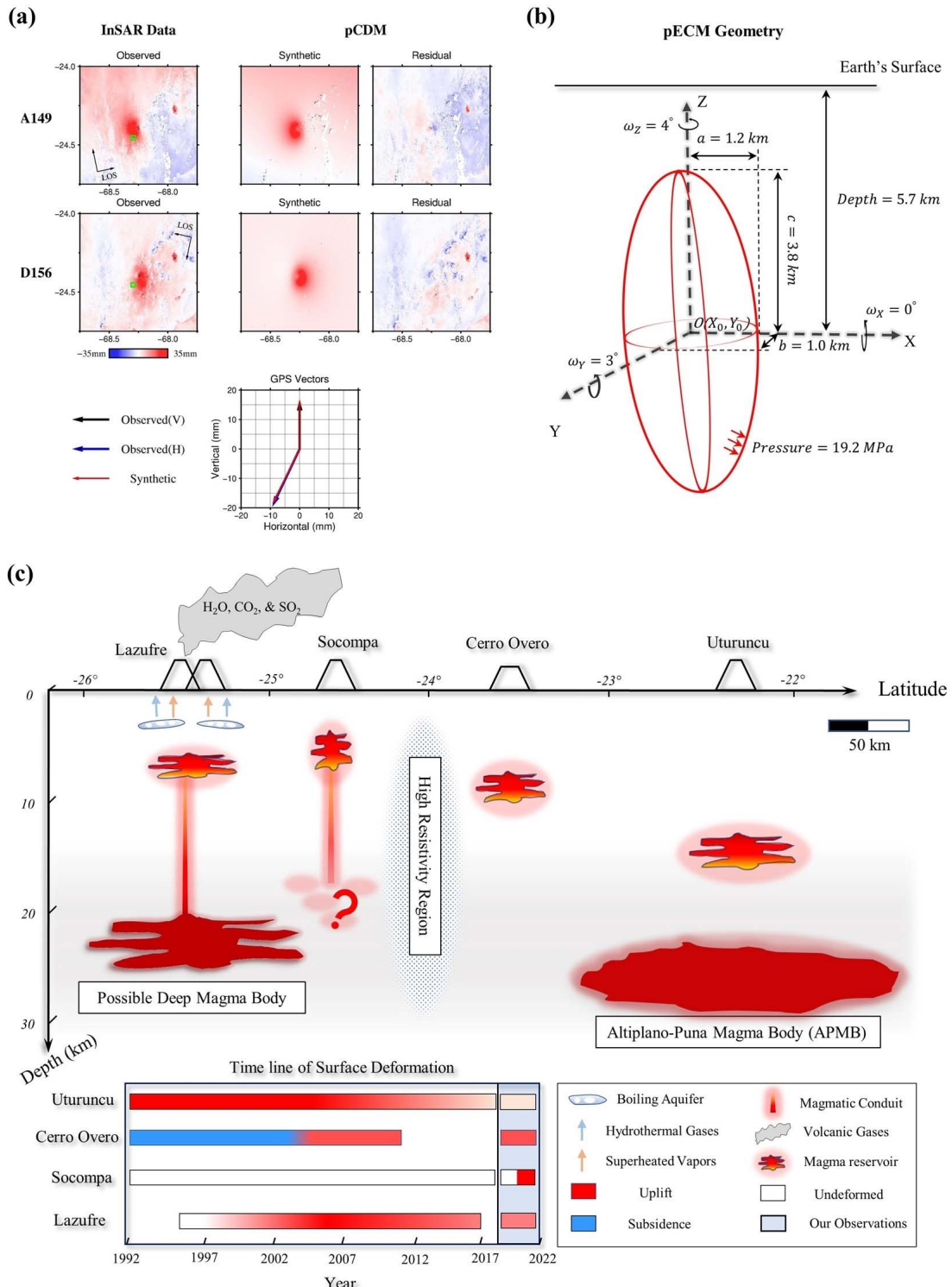
200 **Figure 3.** GPS time series parameter fitting to determine the deformation onset at Socoma volcano. (a) Daily
 201 GPS time series and parameterized fitting using Equation 2, and corresponding residuals. The thick red vertical
 202 line shows the 95% confidence interval of the onset time. The data have been detrended using the MIDAS
 203 algorithm before fitting (Blewitt et al., 2016). (b) Decomposition of East and North directions of GPS data into
 204 movement parallel and perpendicular to the direction of seasonal motion. (c) The relative location of this
 205 SOCM GPS station, using the vertical post onset time cumulative deformation field decomposed from
 206 ascending and descending as the background image.

207 3.2 Volcanic Geodetic Source Modelling

208 As we detect unrest at Socompa for the first time, we explore several source models to
209 explain the observed deformation, including a point pressure source (Mogi, 1958), prolate
210 spheroid (Yang et al., 1988), dipping dike with uniform opening (Okada, 1985), and a point
211 Compound Dislocation Model (pCDM, Nikkhoo et al, 2017; Lundgren et al., 2017). We use
212 the reconstructed post-onset cumulative deformation fields from the InSAR time series (Dec
213 2019 to Oct 2021), and cumulative GPS deformation at SOCM station that has the same time
214 scale as InSAR data, as it improves the signal-to-noise ratio (SNR) of input data and
215 subsequently provides more robust modelling results.

216 We first use a nested uniform downsampling of the InSAR data, with a greater pixel
217 density in the deformation area (Figure S3). Then we use the GBIS software (Bagnardi &
218 Hooper, 2018), a Bayesian approach for the inversion of multiple geodetic data sets that
219 provides the posterior probability density functions of source model parameters, to invert the
220 model parameters. We embed the code of pCDM (Nikkhoo et al., 2017) into the GBIS
221 software so that all models run in the same environment, and use the data uncertainty within
222 the InSAR and GPS observations to weight them during the inversion (Figure S4).

223 Our modelling results show the pCDM fits the observations best (Figure 4 and S5-9).
224 To obtain the equivalent volume change of pCDM, we further use the point Ellipsoidal
225 Cavity Model (pECM, Nikkhoo et al, 2017), a special case of pCDM that is constrained to
226 represent a pressurized ellipsoidal cavity, to perform the inversion using the inferred source
227 location and orientation from pCDM. We find that pCDM (pECM) gives a shallower source
228 depth of ~ 5.7 km and a smaller volume change of $\sim 1.1 \times 10^7 \text{ m}^3$ compared to other models
229 (Table S1).



230

231 **Figure 4.** (a) Volcanic source model of Socampa cumulative uplift (Dec 2019 – Oct 2021) using pCDM. It shows
 232 the modelling results of InSAR and GPS observations. The green box in InSAR observations indicates the
 233 location of the SOCM station. In the GPS panel, the black vertical vector represents the up-component
 234 deformation (\sim 15 mm), while the blue vector signifies the horizontal deformation in the east (\sim 10 mm) and

235 north (~20 mm) directions. (b) Source geometry derived from pECM, which is defined by the source location
236 ($X_0, Y_0, Depth$), the rotation angles around three axes ($\omega_X, \omega_Y, \omega_Z$), the semi-axes along three axes (a, b, c),
237 and the pressure on the cavity walls. Poisson's ratio is 0.25 and shear modulus is 32GPa here. (c) Cartoon
238 depicting the magmatic systems in this region (approximate representation of relative locations), and those
239 timelines of surface deformations from 1992-2021 measured by InSAR and GPS. We plot the approximate
240 depth of magma reservoir of Lazufre, Cerro Overo, and Uturuncu from Henderson et al., 2017, Henderson &
241 Pritchard, 2013, and Henderson & Pritchard, 2017, respectively. We plot the rough depth of a possible deep
242 magma body under Lazufre from Stechern et al., 2017, the shape and depth of APMB from Ward et al., 2014,
243 and the extent of the high resistivity region from Ślęzak et al., 2021. Depth at 0 km means the earth's surface
244 at the local topography (summit elevations: 5,706 m at Lazufre, 6,031 m at Socompa, ~5,000 m at Cerro Overo,
245 and 6,008 m at Uturuncu).

246 **4 Other Displacement Signals**

247 4.1 Volcanic Deformation

248 Several volcanoes have been reported to be deforming in the past few decades (Figure
249 2) and we tie our InSAR observation to the GPS network in this region (Text S3 and Figure
250 S10) to compare our results to these earlier studies. Starting in the north, Uturuncu previously
251 showed a deformation rate of ~15 mm/yr in the 1990s (Fialko & Pearse, 2012; Henderson &
252 Pritchard, 2013), but this gradually slowed in the 2010s (Gottsmann et al., 2017) to a rate of
253 3-5 mm/yr in ~2017 (Lau et al., 2018). In agreement with previous studies, we observe an
254 uplift rate of 2.5 ± 1.8 mm/yr on Uturuncu (2018-2021, Figure S11). Putana displayed short-
255 lived uplift totaling 40 mm displacement in 2009-2010 (Henderson & Pritchard, 2013), whilst
256 we find potential subsidence of -3.9 ± 2.1 mm/yr (Dec 2019-Oct 2021), with an onset which
257 seems coincident with the deformation at Socompa (Figure S12). The deformation signal
258 close to the Cerro Overo, which previously changed from subsidence of -4 mm/yr (1992-
259 2003) to uplift of 5 mm/yr through 2010 on descending track (Henderson & Pritchard, 2013),
260 continues to uplift at a rate of 3.8 ± 2.6 mm/yr (ascending LOS velocity, 2018-2021). Lazufre

261 volcano shows uplift rates of 11.2 ± 1.7 mm/yr (2018-2021, Figure S13), consistent with the
262 trend of surface deformation slowing at this volcano (Henderson & Pritchard, 2013; Remy et
263 al., 2014; Henderson et al., 2017).

264 4.2 Salar Deformation

265 The salar regions, principally the Salar de Atacama and Salar de, appear to show very
266 different behaviours either side of the onset time (Figure 2). However, we find it is mainly
267 due to the misfit to Equation 1 since there no significant linear velocity changes occurred in
268 salars.

269 However, we do find that there is an obvious InSAR phase change in the west of Salar
270 de Atacama and southwest of Salar de Arizaro region, from early to middle 2019 (Figure
271 S14). Since the deforming area matches well with the salar boundaries on both ascending and
272 descending tracks (data are unfiltered) and some small salars in this region have been
273 reported to be deforming in 2003-2008 (Ruch et al., 2012), these patterns indicate real signals
274 instead of artifacts that propagate in the processing chain. This deformation might be related
275 to the extraction of lithium brines (extraction plants have been built in this area), and large
276 groundwater movements (extractions, recharge or caused by tides) in the salar regions during
277 this period (Pritchard, 2003; Liu et al., 2019).

278 **5 Discussion**

279 Since the Socompa uplift started months before the M_w 6.8 intraslab earthquake, we
280 consider a plausible explanation for the sudden uplift to be the ascent of magmatic fluids
281 from a deeper melt source into a shallower reservoir. A magnetotelluric study (Ślezak et al.,
282 2021) in the Atacama region found a high conductivity zone at Socompa (~5 km west of the
283 volcano and spanning 2 km to over 30 km depth), although there is significant uncertainty on
284 this as it is constrained by only one measurement point at Socompa. The crust beneath
285 Socompa and Cerro Overo has not been subject to the same level of study as Uturuncu and

286 the APMB (e.g., Comeau et al., 2016). Deformation at Socompa has some first order
287 similarities to that at Lazufre (~90 km to the South): they have similar source depth (< 10 km)
288 and rate of volume change in order of $10^6 \text{ m}^3/\text{yr}$ (Remy et al., 2014; Henderson et al., 2017).
289 The shallow reservoir and hydrothermal system beneath Lazufre have been suggested to be
290 linked to a possible deep magma body (Budach et al., 2013; Stechern et al., 2017), but there
291 is no independent evidence for this at Socompa.

292 An interesting question here is whether the initiation of uplift at Socompa will
293 maintain a linear rate, decrease exponentially like at Lazufre or whether it will gradually slow
294 and eventually cease. The current geodetic observations show no trace deceleration, which in
295 a purely elastic system would imply a constant pressure increase. Alternatively, it may be too
296 early to detect any decrease in magnitude of a hydraulic connection to a deeper magma
297 supply. Note that the current pressure we obtain from the model is $\sim 19.2 \text{ MPa}$, which is far
298 less than the overpressure required for chamber wall failure (Gerbault et al., 2018).

299 Deformation at Socompa is very consistent with other observations of unrest in the
300 Central Andes (e.g., Pritchard & Simons, 2004a; Henderson & Pritchard, 2013). The
301 deformation rate is low (usually $< 30 \text{ mm/yr}$), and uplift started after an apparently very long
302 period of quiescence (like Lazufre), consistent with deformation taking place on much longer
303 timescales than other parts of the Andes (inter-eruptive and co-eruptive deformation rates are
304 much higher in both the Northern and Southern Andes, e.g., Pritchard & Simons, 2004b;
305 Fournier et al., 2010; Morales Rivera et al., 2016). This means that Holocene activity is not a
306 good basis for assessing whether Central Andean volcanoes have active magmatic systems or
307 are likely to enter a phase of unrest. InSAR measurements of deformation are therefore
308 critical for detection of volcanic unrest. However, volcano deformation in the Central Andes
309 (with the exception of at Sabancaya) is not associated with eruption, reflecting lower rates of

310 reservoir pressurization and therefore lower rates of magma flux that are more conducive to
311 intrusion growth than brittle failure, dyke propagation and magma ascent.

312 **6 Conclusion**

313 Our observations of the first detected unrest at Socompa volcano, Chile, contribute to
314 a picture of low-rate, periodic deformation at Central Andean volcanoes, indicative of
315 magmatic processes that take place on very long time scales. We test several geodetic source
316 models and find a best-fit source depth of \sim 5.7 km and volume change of \sim 5.8 \times 10⁶ m³/yr
317 using a point ellipsoidal source. We capture the onset of deformation at a Central Andean
318 volcano for the first time at high temporal resolution, which allows us to rule out earthquake
319 triggering. This provides a potentially important dataset for assessing the temporal
320 development and therefore origin of such deformation.

321 **Acknowledgement**

322 This work is supported by the UK Natural Environment Research Council (NERC) through
323 the Centre for the Observation and Modelling of Earthquakes, Volcanoes and Tectonics
324 (COMET, <http://comet.nerc.ac.uk>). Figures were made using the Generic Mapping Tools
325 (GMT) (Wessel et al., 2013). The Sentinel-1 InSAR data are copyrighted by the European
326 Space Agency, and are additionally distributed by the Alaska Satellite Facility. This work
327 was undertaken on ARC4, part of the High Performance Computing facilities at the
328 University of Leeds, UK. This work was supported by NERC through the Looking into the
329 Continents from Space (LiCS) large Grant (NE/K010867/1).

330
331 FL acknowledges support from the Great Britain-China Educational Trust. JE and TC
332 acknowledge support from the Royal Society through University Research Fellowships
333 (UF150282 and URF\R1\180088). SE is funded by a NERC Independent Research
334 Fellowship (NE/R015546/1). AH and CNL acknowledge support from the European
335 Research Council (ERC) through the EU Horizon 2020 project DEEPVOLC (grant number
336 866085). FD thanks FONDECYT Iniciacion 11220513 research grant for funding.
337

338 We thank Sofia Parra, Milton Quinteros, Gabriela Herrara, Joaquín Castillo, Scott
339 Henderson, Julie Elliott, and especially Matthew Pritchard (for installing the SOCM station) for
340 their help in retrieving and processing the data of SOCM station.
341

342 **Data Availability Statement**

343 The Sentinel-1 SAR data are copyrighted by the European Space Agency and additionally
344 distributed by the Alaska Satellite Facility Distributed Active Archive Center

345 (<https://earthdata.nasa.gov/eosdis/daacs/asf>). All the GPS data we use is processed by the Nevada
346 Geodetic Laboratory (<http://geodesy.unr.edu>). The InSAR time series fitting and geodetic
347 modelling results are available on Zenodo (<https://doi.org/10.5281/zenodo.7416237>).
348

349 **Reference**

- 350 Agram, P. S., & Simons, M. (2015). A noise model for InSAR time series. *Journal of*
351 *Geophysical Research: Solid Earth*, 120(4), 2752–2771.
352 <https://doi.org/10.1002/2014JB011271>
- 353 Aguilera, F., Apaza, F., Del Carpio, J., Grosse, P., Jiménez, N., Ureta, G., Inostroza, M., Báez,
354 W., Layana, S., Gonzalez, C., Rivera, M., Ortega, M., Gonzalez, R., & Iriarte, R. (2022).
355 Advances in scientific understanding of the Central Volcanic Zone of the Andes: a
356 review of contributing factors. *Bulletin of Volcanology*, 84(3), 1–8.
357 <https://doi.org/10.1007/s00445-022-01526-y>
- 358 Bagnardi, M., & Hooper, A. (2018). Inversion of Surface Deformation Data for Rapid
359 Estimates of Source Parameters and Uncertainties: A Bayesian Approach. *Geochemistry,*
360 *Geophysics, Geosystems*, 19(7), 2194–2211. <https://doi.org/10.1029/2018GC007585>
- 361 Barone, A., Fedi, M., Tizzani, P., & Castaldo, R. (2019). Multiscale analysis of DInSAR
362 measurements for multi-source investigation at uturuncu volcano (Bolivia). *Remote*
363 *Sensing*, 11(6). <https://doi.org/10.3390/rs11060703>
- 364 Biggs, J., Ebmeier, S. K., Aspinall, W. P., Lu, Z., Pritchard, M. E., Sparks, R. S. J., & Mather,
365 T. A. (2014). Global link between deformation and volcanic eruption quantified by
366 satellite imagery. *Nature Communications*, 5. <https://doi.org/10.1038/ncomms4471>
- 367 Biggs, J., & Pritchard, M. E. (2017). Global volcano monitoring: what does it mean when
368 volcanoes deform? *Elements*, 13(1), 17–22. <https://doi.org/10.2113/gselements.13.1.17>
- 369 Blewitt, G., Kreemer, C., Hammond, W. C., & Gazeaux, J. (2016). MIDAS robust trend
370 estimator for accurate GPS station velocities without step detection. *Journal of*
371 *Geophysical Research: Solid Earth*, 121, 2054–2068.
372 <https://doi.org/10.1002/2015JB012552>
- 373 Budach, I., Brasse, H., & Díaz, D. (2013). Crustal-scale electrical conductivity anomaly
374 beneath inflating Lazufre volcanic complex, Central Andes. *Journal of South American*
375 *Earth Sciences*, 42, 144–149. <https://doi.org/10.1016/j.jsames.2012.11.002>
- 376 Chaussard, E., & Amelung, F. (2012). Precursory inflation of shallow magma reservoirs at
377 west Sunda volcanoes detected by InSAR. *Geophysical Research Letters*, 39(21), 6–11.
378 <https://doi.org/10.1029/2012GL053817>
- 379 Comeau, M. J., Unsworth, M. J., & Cordell, D. (2016). New constraints on the magma
380 distribution and composition beneath Volcan Uturuncu and the southern Bolivian
381 Altiplano from magnetotelluric data. *Geosphere*, 12(5), 1391–1421.
382 <https://doi.org/10.1130/GES01277.1>

- 383 Costello, E. K., Halloy, S. R. P., Reed, S. C., Sowell, P., & Schmidt, S. K. (2009). Fumarole-
384 supported islands of biodiversity within a hyperarid, high-elevation landscape on
385 socompa volcano, puna de atacama, andes. In *Applied and Environmental Microbiology*
386 (Vol. 75, Issue 3, pp. 735–747). <https://doi.org/10.1128/AEM.01469-08>
- 387 Díaz, D., Heise, W., & Zamudio, F. (2015). Three-dimensional resistivity image of the
388 magmatic system beneath Lastarria volcano and evidence for magmatic intrusion in the
389 back arc (northern Chile). *Geophysical Research Letters*, 42(13), 5212–5218.
390 <https://doi.org/10.1002/2015GL064426>
- 391 Ebmeier, S. K., Andrews, B. J., Araya, M. C., Arnold, D. W. D., Biggs, J., Cooper, C.,
392 Cottrell, E., Furtney, M., Hickey, J., Jay, J., Lloyd, R., Parker, A. L., Pritchard, M. E.,
393 Robertson, E., Venzke, E., & Williamson, J. L. (2018). Synthesis of global satellite
394 observations of magmatic and volcanic deformation: implications for volcano
395 monitoring & the lateral extent of magmatic domains. *Journal of Applied Volcanology*,
396 7(1). <https://doi.org/10.1186/s13617-018-0071-3>
- 397 Fariás, M. E., Rascovan, N., Toneatti, D. M., Albarracín, V. H., Flores, M. R., Poiré, D. G.,
398 Collavino, M. M., Aguilar, O. M., Vazquez, M. P., & Polerecky, L. (2013). The
399 Discovery of Stromatolites Developing at 3570 m above Sea Level in a High-Altitude
400 Volcanic Lake Socompa, Argentinean Andes. *PLoS ONE*, 8(1).
401 <https://doi.org/10.1371/journal.pone.0053497>
- 402 Fialko, Y., & Pearse, J. (2012). Sombrero uplift above the Altiplano-Puna magma body:
403 Evidence of a ballooning mid-crustal diapir. *Science*, 338(6104), 250–252.
404 <https://doi.org/10.1126/science.1226358>
- 405 Fournier, T. J., Pritchard, M. E., & Riddick, S. N. (2010). Duration, magnitude, and
406 frequency of subaerial volcano deformation events: New results from Latin America
407 using InSAR and a global synthesis. *Geochemistry, Geophysics, Geosystems*, 11(1).
408 <https://doi.org/10.1029/2009GC002558>
- 409 Gaete, A., Walter, T. R., Bredemeyer, S., Zimmer, M., Kujawa, C., Franco Marin, L., San
410 Martin, J., & Bucarey Parra, C. (2020). Processes culminating in the 2015 phreatic
411 explosion at Lascar volcano, Chile, evidenced by multiparametric data. *Natural Hazards
412 and Earth System Sciences*, 20(2), 377–397. <https://doi.org/10.5194/nhess-20-377-2020>
- 413 Gerbault, M., Hassani, R., Novoa Lizama, C., & Souche, A. (2018). Three-Dimensional
414 Failure Patterns Around an Inflating Magmatic Chamber. *Geochemistry, Geophysics,
415 Geosystems*, 19(3), 749–771. <https://doi.org/10.1002/2017GC007174>
- 416 Gottsmann, J., Blundy, J., Henderson, S., Pritchard, M. E., & Sparks, R. S. J. (2017).
417 Thermomechanical modeling of the altiplano-puna deformation anomaly:
418 Multiparameter insights into magma mush reorganization. *Geosphere*, 13(4), 1042–1045.
419 <https://doi.org/10.1130/GES01420.1>
- 420 Halloy, S. (1991). Islands of Life at 6000 M Altitude: The Environment of the Highest
421 Autotrophic Communities on Earth (Socompa Volcano, Andes). *Arctic and Alpine
422 Research*, 23(3), 247–262. <https://doi.org/10.1080/00040851.1991.12002843>

- 423 Henderson, S. T., Delgado, F., Elliott, J., Pritchard, M. E., & Lundgren, P. R. (2017).
424 Decelerating uplift at Lazufre volcanic center, Central Andes, from A. D. 2010 to 2016,
425 and implications for geodetic models. *Geosphere*, 13(5), 1489–1505.
426 <https://doi.org/10.1130/GES01441.1>
- 427 Henderson, S. T., & Pritchard, M. E. (2013). Decadal volcanic deformation in the central
428 andes volcanic zone revealed by InSAR time series. *Geochemistry, Geophysics,
429 Geosystems*, 14(5), 1358–1374. <https://doi.org/10.1002/ggge.20074>
- 430 Henderson, S. T., & Pritchard, M. E. (2017). Time-dependent deformation of Uturuncu
431 volcano , Bolivia , constrained by GPS and InSAR measurements and implications for
432 source models. *Geosphere*, 13(6), 1834–1854. <https://doi.org/10.1130/GES01203.1>
- 433 Hickey, J., Gottsmann, J., & Del Potro, R. (2013). The large-scale surface uplift in the
434 Altiplano-Puna region of Bolivia: A parametric study of source characteristics and
435 crustal rheology using finite element analysis. *Geochemistry, Geophysics, Geosystems*,
436 14(3). <https://doi.org/10.1002/ggge.20057>
- 437 Hooper, A., Segall, P., & Zebker, H. (2007). Persistent scatterer interferometric synthetic
438 aperture radar for crustal deformation analysis, with application to Volcán Alcedo,
439 Galápagos. *Journal of Geophysical Research: Solid Earth*, 112(7), 1–21.
440 <https://doi.org/10.1029/2006JB004763>
- 441 Jay, J. A., Welch, M., Pritchard, M. E., Mares, P. J., Mnich, M. E., Melkonian, A. K.,
442 Aguilera, F., Naranjo, J. A., Sunagua, M., & Clavero, J. (2013). Volcanic hotspots of the
443 central and southern andes as seen from space by ASTER and MODVOLC between the
444 years 2000 and 2010. *Geological Society Special Publication*, 380(1), 161–185.
445 <https://doi.org/10.1144/SP380.1>
- 446 J. Ruch, T.R. Walter (2010), Relationship between the InSAR-measured uplift, the structural
447 framework, and the present-day stress field at Lazufre volcanic area, central
448 Andes. *Tectonophysics*, 492 (1–4), 133-140, <https://doi.org/10.1016/j.tecto.2010.06.003>.
- 449 Lau, N., Tymofyeyeva, E., & Fialko, Y. (2018). Variations in the long-term uplift rate due to
450 the Altiplano–Puna magma body observed with Sentinel-1 interferometry. *Earth and
451 Planetary Science Letters*, 491, 43–47. <https://doi.org/10.1016/j.epsl.2018.03.026>
- 452 Lazecký, M., Spaans, K., González, P. J., Maghsoudi, Y., Morishita, Y., Albino, F., Elliott, J.,
453 Greenall, N., Hatton, E., Hooper, A., Juncu, D., McDougall, A., Walters, R. J., Watson,
454 C. S., Weiss, J. R., & Wright, T. J. (2020). LiCSAR: An automatic InSAR tool for
455 measuring and monitoring tectonic and volcanic activity. *Remote Sensing*, 12(15).
456 <https://doi.org/10.3390/RS12152430>
- 457 Liu, F., Elliott, J. R., Craig, T. J., Hooper, A., & Wright, T. J. (2021). Improving the
458 Resolving Power of InSAR for Earthquakes Using Time Series: A Case Study in Iran.
459 *Geophysical Research Letters*, 48(14). <https://doi.org/10.1029/2021GL093043>
- 460 Liu, W., Agusdinata, D. B., & Myint, S. W. (2019). Spatiotemporal patterns of lithium
461 mining and environmental degradation in the Atacama Salt Flat, Chile. *International*

- 462 *Journal of Applied Earth Observation and Geoinformation*, 80, 145–156.
463 <https://doi.org/10.1016/j.jag.2019.04.016>
- 464 Lundgren, P., Nikkhoo, M., Samsonov, S. V., Milillo, P., Gil-Cruz, F., & Lazo, J. (2017).
465 Source model for the Copahue volcano magma plumbing system constrained by InSAR
466 surface deformation observations. *Journal of Geophysical Research: Solid Earth*, 122(7),
467 5729–5747. <https://doi.org/10.1002/2017JB014368>
- 468 Lupi, M., Frehner, M., Weis, P., Skelton, A., Saenger, E. H., Tisato, N., Geiger, S., Chiodini,
469 G., & Driesner, T. (2017). Regional earthquakes followed by delayed ground uplifts at
470 Campi Flegrei Caldera, Italy: Arguments for a causal link. *Earth and Planetary Science
471 Letters*, 474, 436–446. <https://doi.org/10.1016/j.epsl.2017.07.006>
- 472 MacQueen, P., Delgado, F., Reath, K., Pritchard, M. E., Bagnardi, M., Milillo, P., Lundgren,
473 P., Macedo, O., Aguilar, V., Ortega, M., Anccasi, R., Lazarte Zerpa, I. A., & Miranda, R.
474 (2020). Volcano-Tectonic Interactions at Sabancaya Volcano, Peru: Eruptions,
475 Magmatic Inflation, Moderate Earthquakes, and Fault Creep. *Journal of Geophysical
476 Research: Solid Earth*, 125(5), 1–25. <https://doi.org/10.1029/2019JB019281>
- 477 Mogi, K. (1958). Relations between the eruptions of various volcanoes and the deformations
478 of the ground surfaces around them, *Bull. Earthquake Res. Inst.*, Tokyo, 36, 99–134
- 479 Morales Rivera, A. M., F. Amelung, and P. Mothes (2016), Volcano deformation survey over
480 the Northern and Central Andes with ALOS InSAR time series, *Geochem. Geophys.
481 Geosyst.*, 17, 2869–2883, doi:10.1002/2016GC006393. Nikkhoo, M., Walter, T. R.,
482 Lundgren, P. R., & Prats-Iraola, P. (2017). Compound dislocation models (CDMs) for
483 volcano deformation analyses. *Geophysical Journal International*, 208(2), 877–894.
484 <https://doi.org/10.1093/gji/ggw427>
- 485 Okada, Y. (1992). Internal deformation due to shear and tensile faults in a half-space. *Bulletin
486 - Seismological Society of America*, 82(2), 1018–1040.
487 <https://doi.org/10.1785/bssa0820021018>
- 488 Osmanoğlu, B., Sunar, F., Wdowinski, S., & Cabral-Cano, E. (2016). Time series analysis of
489 InSAR data: Methods and trends. *ISPRS Journal of Photogrammetry and Remote
490 Sensing*, 115, 90–102. <https://doi.org/10.1016/j.isprsjprs.2015.10.003>
- 491 Pearse, J., and P. Lundgren (2013), Source model of deformation at Lazufre volcanic center,
492 central Andes, constrained by InSAR time series, *Geophys. Res. Lett.*, 40, 1059–1064,
493 doi:10.1002/grl.50276
- 494 Perkins, J. P., Ward, K. M., de Silva, S. L., Zandt, G., Beck, S. L., & Finnegan, N. J. (2016).
495 Surface uplift in the Central Andes driven by growth of the Altiplano Puna Magma
496 Body. *Nature Communications*, 7. [htfltps://doi.org/10.1038/ncomms13185](https://doi.org/10.1038/ncomms13185)
- 497 Poland, M. P., & Zebker, H. A. (2022). Volcano geodesy using InSAR in 2020: the past and
498 next decades. *Bulletin of Volcanology*, 84(3). <https://doi.org/10.1007/s00445-022-01531-1>

- 500 Pritchard, M. E. (2003). Recent Crustal Deformation in West-Central South America,
501 (Doctoral dissertation). Retrieved from Caltch THESIS.
502 (<https://resolver.caltech.edu/CaltechETD:etd-06022003-105512>). California Blvd,
503 Pasadena, CA: California Institute of Technology
- 504 Pritchard, M. E., de Silva, S. L., Michelfelder, G., Zandt, G., McNutt, S. R., Gottsmann, J.,
505 West, M. E., Blundy, J., Christensen, D. H., Finnegan, N. J., Minaya, E., Sparks, R. S. J.,
506 Sunagua, M., Unsworth, M. J., Alvizuri, C., Comeau, M. J., del Potro, R., Diaz, D., Diez,
507 M., ... Ward, K. M. (2018). Synthesis: PLUTONS: Investigating the relationship
508 between pluton growth and volcanism in the Central Andes. *Geosphere*, 14(3), 954–982.
509 <https://doi.org/10.1130/GES01578.1>
- 510 Pritchard, M. E., Jay, J. A., Aron, F., Henderson, S. T., & Lara, L. E. (2013). Subsidence at
511 southern Andes volcanoes induced by the 2010 Maule, Chile earthquake. *Nature
512 Geoscience*, 6(8), 632–636. <https://doi.org/10.1038/ngeo1855>
- 513 Pritchard, M. E., Mather, T. A., McNutt, S. R., Delgado, F. J., & Reath, K. (2019). Thoughts
514 on the criteria to determine the origin of volcanic unrest as magmatic or non-magmatic.
515 *Philosophical Transactions of the Royal Society A: Mathematical, Physical and
516 Engineering Sciences*, 377(2139). <https://doi.org/10.1098/rsta.2018.0008>
- 517 Pritchard, M. E., & Simons, M. (2002). A satellite geodetic survey of large-scale deformation
518 of volcanic centres in the central Andes. *Nature*, 418(6894), 167–171.
519 <https://doi.org/10.1038/nature00872>
- 520 Pritchard, M. E., & Simons, M. (2004a). An InSAR-based survey of volcanic deformation in
521 the central Andes. *Geochemistry, Geophysics, Geosystems*, 5(2), 1–42.
522 <https://doi.org/10.1029/2003GC000610>
- 523 Pritchard, M. E., & Simons, M. (2004b). An InSAR-based survey of volcanic deformation in
524 the southern Andes. *Geophysical Research Letters*, 31(15), 1–4.
525 <https://doi.org/10.1029/2004GL020545>
- 526 Reath, K., Pritchard, M., Poland, M., Delgado, F., Carn, S., Coppola, D., Andrews, B.,
527 Ebmeier, S. K., Rumpf, E., Henderson, S., Baker, S., Lundgren, P., Wright, R., Biggs, J.,
528 Lopez, T., Wauthier, C., Moruzzi, S., Alcott, A., Wessels, R., ... Bagnardi, M. (2019).
529 Thermal, Deformation, and Degassing Remote Sensing Time Series (CE 2000–2017) at
530 the 47 most Active Volcanoes in Latin America: Implications for Volcanic Systems.
531 *Journal of Geophysical Research: Solid Earth*, 124(1), 195–218.
532 <https://doi.org/10.1029/2018JB016199>
- 533 Remy, D., Froger, J. L., Perfettini, H., Bonvalot, S., Gabalda, G., Albino, F., Cayol, V.,
534 Legrand, D., & De, M. (2014). Persistent uplift of the Lazufre volcanic complex
535 (Central Andes): New insights from PCAIM inversion of InSAR time series and GPS
536 data. *Geochemistry, Geophysics, Geosystems*, 15, 3591–3611.
537 <https://doi.org/10.1002/2014GC005370>
- 538 Richter, N., Salzer, J.T., de Zeeuw-van Dalfsen, E., Perissin, D. and Walter, T.R. (2018).
539 Constraints on the geomorphological evolution of the nested summit craters of Láschar

- 540 volcano from high spatio-temporal resolution TerraSAR-X interferometry. *Bulletin of*
541 *Volcanology*. <https://doi.org/10.1007/s00445-018-1195-3>
- 542 Ruch, J., Warren, J. K., Risacher, F., Walter, T. R., & Lanari, R. (2012). Salt lake
543 deformation detected from space. *Earth and Planetary Science Letters*, 331–332, 120–
544 127. <https://doi.org/10.1016/j.epsl.2012.03.009>
- 545 Ślęzak, K., Díaz, D., Vargas, J. A., Cordell, D., Reyes-Cordova, F., & Segovia, M. J. (2021).
546 Magnetotelluric image of the Chilean subduction zone in the Salar de Atacama region
547 (23°–24°S): Insights into factors controlling the distribution of volcanic arc magmatism.
548 *Physics of the Earth and Planetary Interiors*, 318(October 2020).
549 <https://doi.org/10.1016/j.pepi.2021.106765>
- 550 Stebel, K., Amigo, A., Thomas, H., & Prata, A. J. (2014). First estimates of fumarolic SO₂
551 fluxes from Putana volcano, Chile, using an ultraviolet imaging camera. *Journal of*
552 *Volcanology and Geothermal Research*, 300, 112–120.
553 <https://doi.org/10.1016/j.jvolgeores.2014.12.021>
- 554 Stechern, A., Just, T., Holtz, F., Blume-Oeste, M., & Namur, O. (2017). Decoding magma
555 plumbing and geochemical evolution beneath the Lastarria volcanic complex (Northern
556 Chile)—Evidence for multiple magma storage regions. *Journal of Volcanology and*
557 *Geothermal Research*, 338, 25–45. <https://doi.org/10.1016/j.jvolgeores.2017.03.018>
- 558 Takada, Y., & Fukushima, Y. (2013). Volcanic subsidence triggered by the 2011 Tohoku
559 earthquake in Japan. *Nature Geoscience*, 6(8), 637–641.
560 <https://doi.org/10.1038/ngeo1857>
- 561 Yang, X. M., Davis, P. M., & Dieterich, J. H. (1988). Deformation from inflation of a dipping
562 finite prolate spheroid in an elastic half-space as a model for volcanic stressing. *Journal*
563 *of Geophysical Research*, 93(B5), 4249–4257.
564 <https://doi.org/10.1029/JB093iB05p04249>
- 565 Yu, C., Li, Z., Penna, N. T., & Crippa, P. (2018). Generic Atmospheric Correction Model for
566 Interferometric Synthetic Aperture Radar Observations. *Journal of Geophysical*
567 *Research: Solid Earth*, 123(10), 9202–9222. <https://doi.org/10.1029/2017JB015305>
- 568 Wadge, G., Francis, P. W., & Ramirez, C. F. (1995). The Socompa collapse and avalanche
569 event. In *Journal of Volcanology and Geothermal Research* (Vol. 66).
- 570 Ward, K. M., Zandt, G., Beck, S. L., Christensen, D. H., & McFarlin, H. (2014). Seismic
571 imaging of the magmatic underpinnings beneath the Altiplano-Puna volcanic complex
572 from the joint inversion of surface wave dispersion and receiver functions. *Earth and*
573 *Planetary Science Letters*, 404, 43–53. <https://doi.org/10.1016/j.epsl.2014.07.022>
- 574 Wessel, P., Smith, W. H. F., Scharroo, R., Luis, J., & Wobbe, F. (2013). Generic mapping
575 tools: Improved version released. *Eos*, 94(45), 409–410.
576 <https://doi.org/10.1002/2013EO450001>

577 Yunjun, Z., Amelung, F., & Aoki, Y. (2021). Imaging the Hydrothermal System of Kirishima
578 Volcanic Complex With L-Band InSAR Time Series. *Geophysical Research Letters*,
579 48(11). <https://doi.org/10.1029/2021GL092879>

580 **References From the Supporting Information**

581 Ansari, H., De Zan, F., & Parizzi, A. (2020). Study of Systematic Bias in Measuring Surface
582 Deformation with SAR Interferometry. *IEEE Transactions on Geoscience and Remote
583 Sensing, December*, 1–12. <https://doi.org/10.1109/TGRS.2020.3003421>

584 Bekaert, D. P. S., Walters, R. J., Wright, T. J., Hooper, A. J., & Parker, D. J. (2015).
585 Statistical comparison of InSAR tropospheric correction techniques. *Remote Sensing of
586 Environment, 170*, 40–47. <https://doi.org/10.1016/j.rse.2015.08.035>

587 Hussain, E., Hooper, A., Wright, T. J., Walters, R. J., & Bekaert, D. P. S. (2016). Interseismic
588 strain accumulation across the central North Anatolian Fault from iteratively unwrapped
589 InSAR measurements. *Journal of Geophysical Research: Solid Earth*.
590 <https://doi.org/10.1002/2016JB013108>

591 Maghsoudi, Y., Hooper, A. J., Wright, T. J., Lazecky, M., & Ansari, H. (2022).
592 Characterizing and correcting phase biases in short-term, multilooked interferograms.
593 *Remote Sensing of Environment, 275*. <https://doi.org/10.1016/j.rse.2022.113022>

594 Pavez, A., Remy, D., Bonvalot, S., Diament, M., Gabalda, G., Froger, J. L., Julien, P.,
595 Legrand, D., & Moisset, D. (2006). Insight into ground deformations at Lascar volcano
596 (Chile) from SAR interferometry, photogrammetry and GPS data: Implications on
597 volcano dynamics and future space monitoring. *Remote Sensing of Environment, 100*(3),
598 307–320. <https://doi.org/10.1016/j.rse.2005.10.013>

599 Purcell, V., Reddin, E., Ebmeier, S., González, P. J., Watson, A., Morishita, Y., & Elliott, J.
600 (2022). Nearly Three Centuries of Lava Flow Subsidence at Timanfaya, Lanzarote.
601 *Geochemistry, Geophysics, Geosystems, 23*(10). <https://doi.org/10.1029/2022gc010576>

602 Webster, R., & Oliver, M. A. (2007). Geostatistics for environmental scientists (2nd ed.).
603 John Wiley & Sons. <https://doi.org/10.1002/9780470517277>



Geophysics Research Letter

Supporting Information for

**Unrest Detected at Socompa Volcano, Northern Chile, from Geodetic
Observations**

F. Liu¹, J. R. Elliott¹, S. K. Ebmeier¹, T. J. Craig¹, A. Hooper¹,

C. Novoa Lizama¹, and F. Delgado²

¹COMET, School of Earth and Environment, University of Leeds, Leeds, United Kingdom

²Department of Geology and Centro de Excelencia en Geotermia Andina, Universidad de Chile, Santiago, Chile

Contents of this file

Text S1 to S3

Figures S1 to S14

Table S1 to S2

Additional Supporting Information (Files uploaded separately)

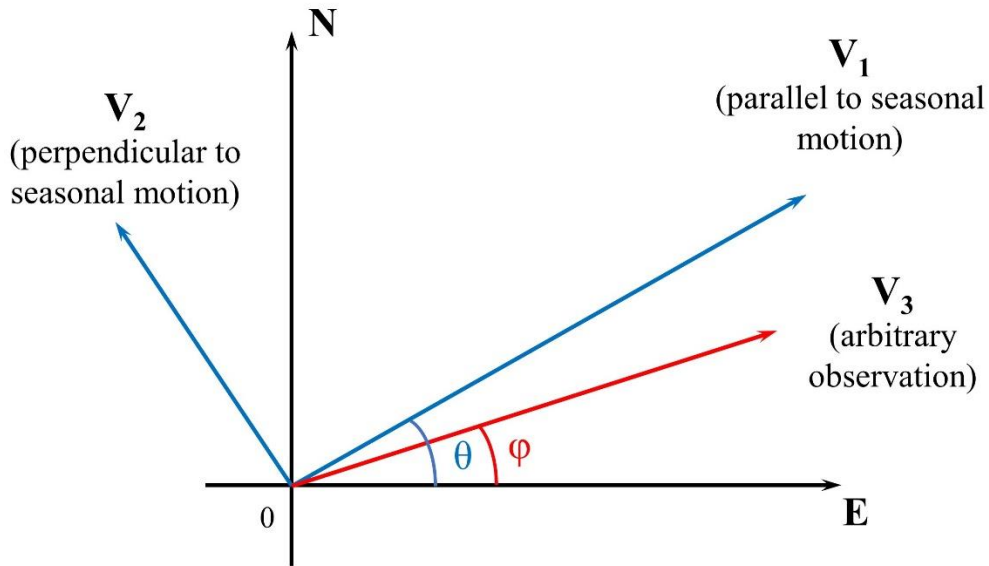
Introduction

Text S1. InSAR processing details

We use the LiCSAR processing chain to form interferograms with multilooking (4 in azimuth and 20 in range), but no further spatial filtering, using Sentinel-1 Interferometric Wide (IW) swath mode Single Look Complex (SLC) images and the Digital Elevation Model (DEM) from the Shuttle Radar Topography Mission (SRTM) 1 arcsec. We form interferogram networks by connecting each image to 10 subsequent acquisitions (6-60 days temporal interferogram, assuming revisiting time is 6 days). We then use the StaMPS software to perform time series analysis, which includes a) resampling pixels to 500 m resolution to reduce data volume, b) application of GACOS correction for tropospheric artefacts using the TRAIN software (Bekaert et al., 2015), c) unwrapping iteratively to reduce unwrapping errors by checking for phase consistency (Hussain et at., 2016), and finally d) using only longer temporal interferograms (48-60 days) for the small baseline inversion to reduce the potential impact of the fading signal (Ansari et al., 2020; Maghsoudi et al., 2022; Purcell et al., 2022).

Text S2. GPS vector decomposition

We can decompose any vectors in a two-dimensional space into two orthogonal vectors. Considering the GPS horizontal displacement, we have the conventional orthogonal coordinates of North and East components, to indicate the GPS position. It is also possible to decompose an arbitrary GPS observation into another orthogonal coordinate system instead of the North-East one. As the figure shown here, we could decompose the vector \mathbf{V}_3 , an arbitrary observation, into the \mathbf{V}_1 (displacement parallel to the direction of seasonal motion), and \mathbf{V}_2 (displacement perpendicular to the direction of seasonal motion) coordinates.



After the decomposition, we have

$$\begin{aligned}\delta_1 &= |\mathbf{V}_3| \cos(\theta - \varphi) \\ \delta_2 &= |\mathbf{V}_3| \sin(\theta - \varphi)\end{aligned}$$

where δ_1 and δ_2 represent the displacement parallel and perpendicular to the direction of seasonal motion, respectively, θ is the angle between \mathbf{V}_1 and \mathbf{E} , and φ is the angle between \mathbf{V}_3 and \mathbf{E} .

Since the direction of seasonal displacement varies throughout the year, to determine the angle θ , we calculate the seasonal direction at time t using the following equation:

$$\theta(t) = \tan^{-1}\left(\frac{|\mathbf{N}(t)|}{|\mathbf{E}(t)|}\right)$$

As the first three years of the horizontal GPS time series of the SOCM site are dominated by seasonal signals, we first calculate θ for each day in the first three years, then average the results of the three years, and finally get the value of θ on each day throughout a year. After obtaining the seasonal direction, we then decompose the horizontal GPS time series into the displacement parallel and perpendicular to the direction of seasonal motion.

Text S3. Tying InSAR and GNSS observation

Here we use all available continuous GPS sites from the database of the Nevada Geodetic Laboratory (Figure S10). We adopt the linear velocity calculated by the Nevada Geodetic Laboratory, using South America Plate as the reference frame.

We first derive the InSAR velocity map from the time series data, and average the values of the pixels surrounding the GPS sites (a circle with a radius of 3 km centred on it, ~120 pixels) as the corresponding velocity value of InSAR data. We then remove a spatial linear ramp in the east and north direction from the InSAR velocity map to minimize the relative difference between InSAR and GNSS, on ascending and descending respectively. Finally, based on this deramped InSAR velocity map and assuming no deformation signals on the north component, we can obtain the uplifting velocity of any pixels that are covered by both tracks by decomposing the InSAR velocity map into the east-west and vertical direction by solving the following formula:

$$\begin{bmatrix} U_{asc} & E_{asc} \\ U_{dsc} & E_{dsc} \end{bmatrix} \begin{bmatrix} V_U \\ V_E \end{bmatrix} = \begin{bmatrix} V_{asc} \\ V_{dsc} \end{bmatrix}$$

where U and E are the up and east components of the line of sight (LOS) vector, respectively.

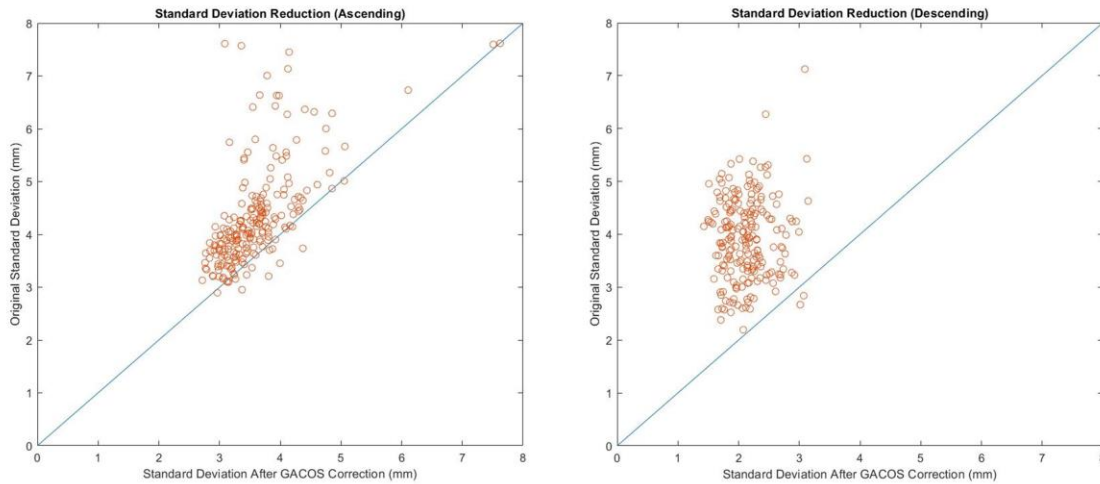


Figure S1. Standard deviation reduction of interferograms after the GACOS correction on ascending and descending track data, respectively. The red dots represent each epoch on time series, and the blue line is the identity line where any dots above it means an improvement after the GACOS correction. Here the average standard error reductions are 16.9% and 45.7% for ascending and descending, respectively.

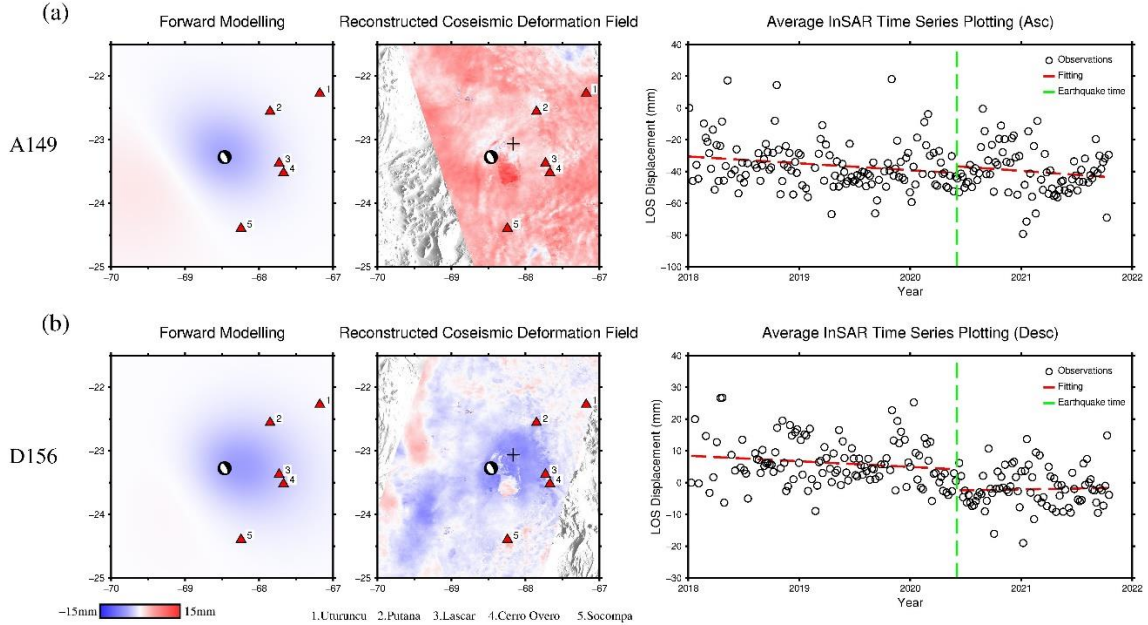


Figure S2. Coseismic deformation field of the M_w 6.8 earthquake reconstruction by InSAR time series fitting. (a) Data of ascending track. From left to right, the forward modelling from the USGS solution (strike: 332° , Dip: 59° , Rake: -94° , centroid depth: 112 km, Moment: 2.29×10^{19} N-m), the reconstructed coseismic deformation field, and the average InSAR time series of peak displacement pixels. (b) Same as (a) but for the descending track. For the forward modelling, we assume a uniform dislocation embedded in an isotropic elastic half-space, faults are equal in width and length, the slip-to-length ratio is set to 1.5×10^{-5} for this interplate earthquake, and the rigidity value used here for moment calculation is 75 GPa. The epicentre of the earthquake is indicated by the black focal mechanism, and volcanoes are marked by red triangles. On the reconstructed coseismic deformation field, the location of peak displacement pixels is marked by a plus symbol. The red patch close to the southeastern point of the epicentre marked (which is observed on both tracks) indicates the shape of Salar de Atacama, and has different behaviour in the time series. In all figures, positive values mean movements towards the satellite.

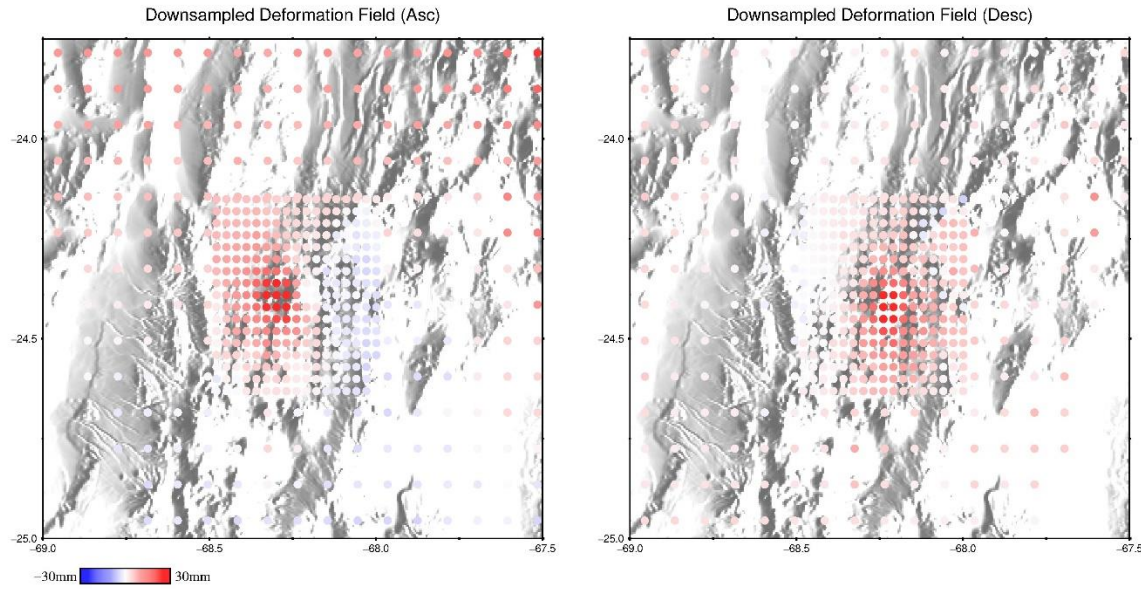


Figure S3. Uniform downsampling of InSAR data for GBIS input. We use a larger pixel density over the Socomba deformation area, resulting in 485 pixels on both the ascending and descending tracks of data.

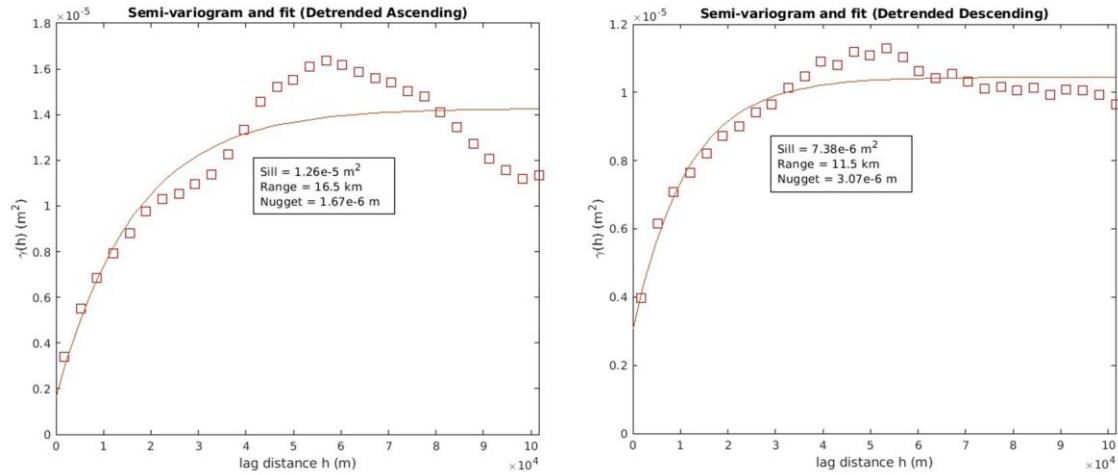


Figure S4. Semi-variogram fitting for post-onset cumulative deformation fields on ascending and descending track using the GBIS software. Errors in the InSAR data can be simulated using an exponential function fitted to the isotropic experimental semi-variogram (Webster & Oliver, 2007), and the lower sill value of the fitted results indicates the higher the signal-to-noise ratio. We use this semi-variogram fitting to calculate the covariance matrix of the InSAR data during the inversion. While for the GPS data covariance matrix, it is obtained from the standard deviations by fitting the equation 2 in the main text.

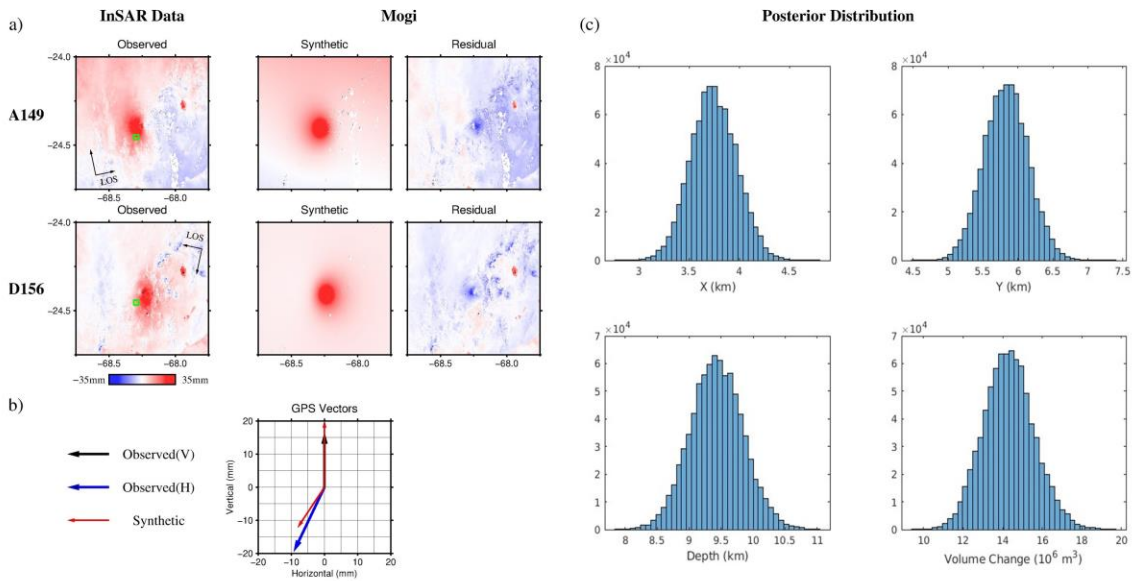


Figure S5. Volcanic source model of Socomba cumulative uplift (Dec 2019 – Oct 2021) using the Mogi model. (a) Modelling results of InSAR observations. The green box indicates the location of the SOCM site. (b) Modelling results of GPS observations. The black vertical vector represents the up component of GPS deformation (~15 mm), while the blue vector signified the horizontal deformation in the east and north directions (here moving ~10 mm west and ~20 mm south). (c) Posterior distributions for all parameters, where X, Y, and Depth indicate the source location reference to the SOCM site (northeast direction), and V represents the volume change (here $\sim 1.4 \times 10^7 \text{ m}^3$).

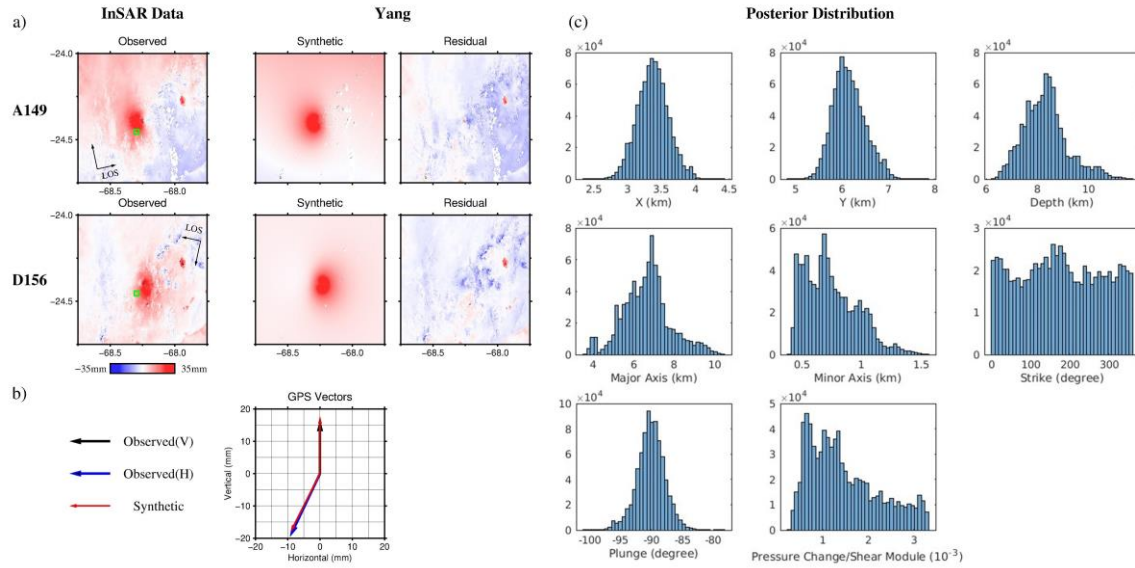


Figure S6. Same as Figure S5 but using Yang model. (c) Semi-major and Semi-minor are the lengths of the two axes, Strike value is the angle of major semi-axis with respect to North, and the Plunge value is the inclination angle of major semi-axis with respect to horizontal. The volume change of the Yang model is $\sim 1.6 \times 10^7 \text{ m}^3$.

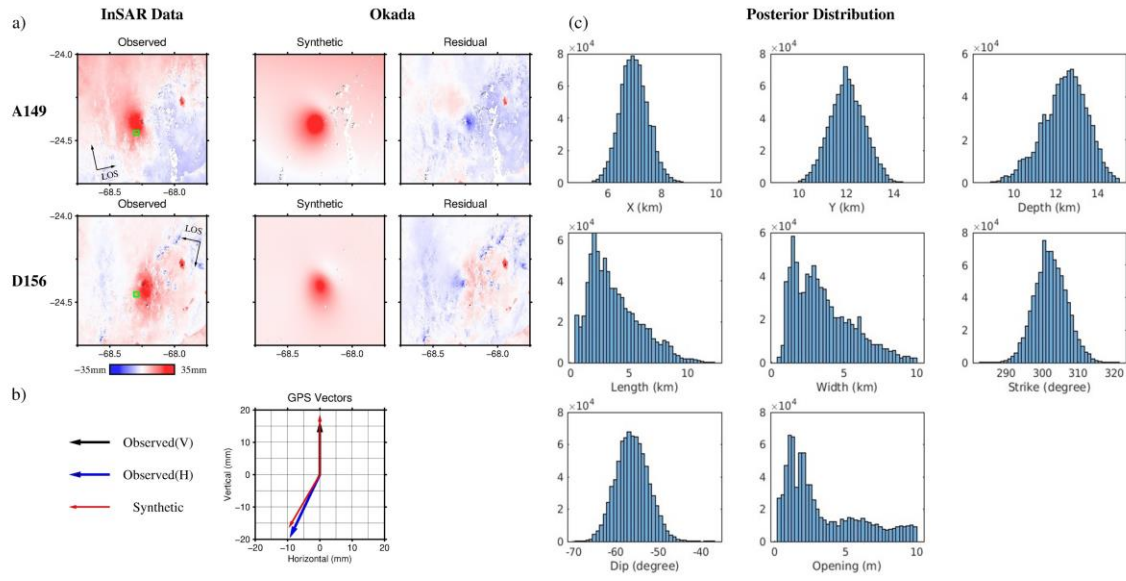


Figure S7. Same as Figure S5 but using Okada model. The volume change of the Okada model is $\sim 2.2 \times 10^7 \text{ m}^3$.

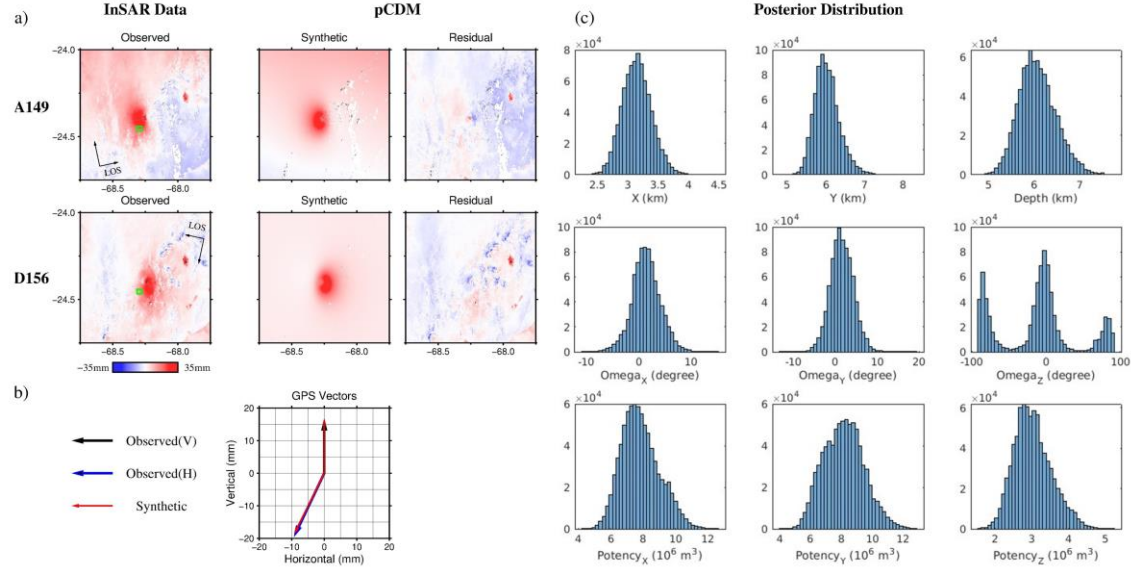


Figure S8. Same as Figure S5 but using pCDM model. (c) $\Omega_{x,y,z}$ are the rotation angles around three axes, and $Potency_{x,y,z}$ are the potencies of the point dislocations on three directions, respectively. Here the bimodal distribution of the rotation angles around the Z axes indicates similar values of potency in the X and Y direction. The total potency of the pCDM, which is defined as the product of dislocation surface area and opening and is a totally different concept from volume change, is $\sim 1.8 \times 10^7$ m³ by summing the potency values in three directions.

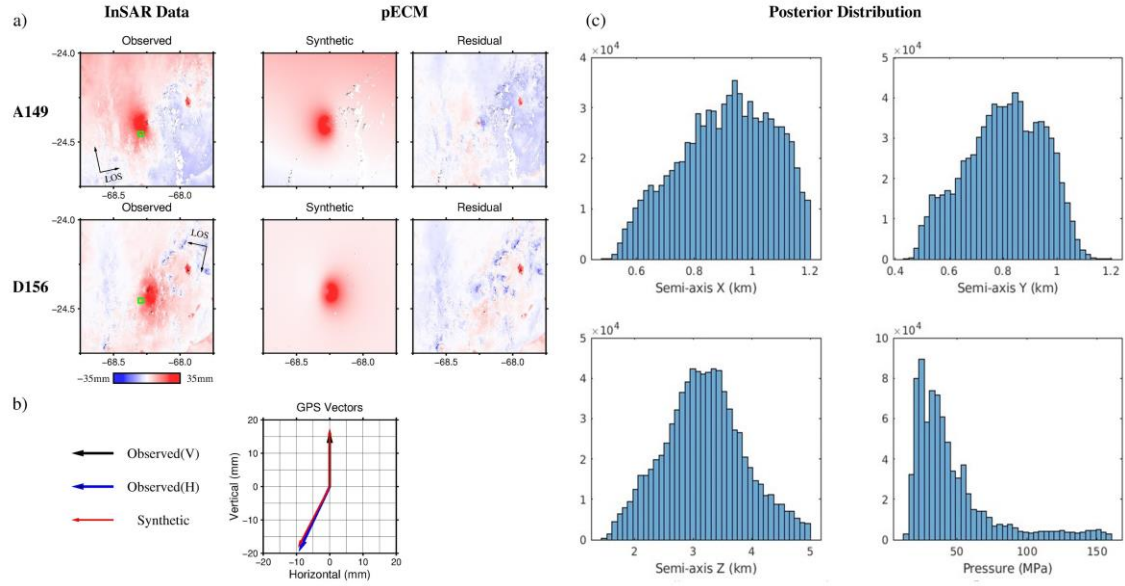


Figure S9. Same as Figure S5 but using pECM model. We use the inferred source location and orientation from pCDM to perform the inversion. The total potency and volume change of the pECM are $\sim 1.8 \times 10^7 \text{ m}^3$ and $\sim 1.1 \times 10^7 \text{ m}^3$, respectively.

Post Onset Time Cumulative InSAR Displacement (Desc)

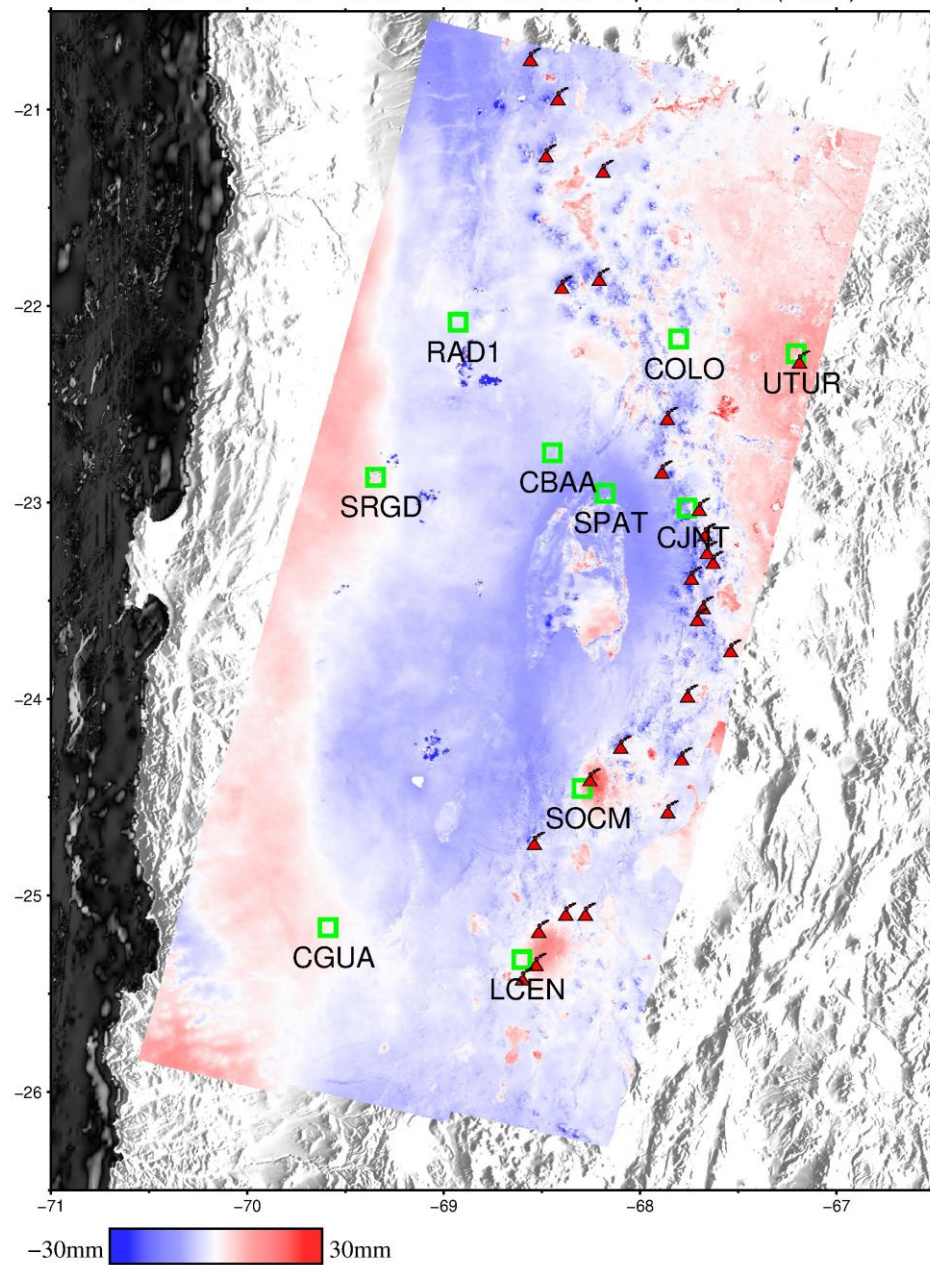


Figure S10. The locations of continuous GPS sites that were used to tie InSAR data, using the descending post onset time cumulated deformation field and topography map as the background image. All GPS data are obtained from the database of the Nevada Geodetic Laboratory.

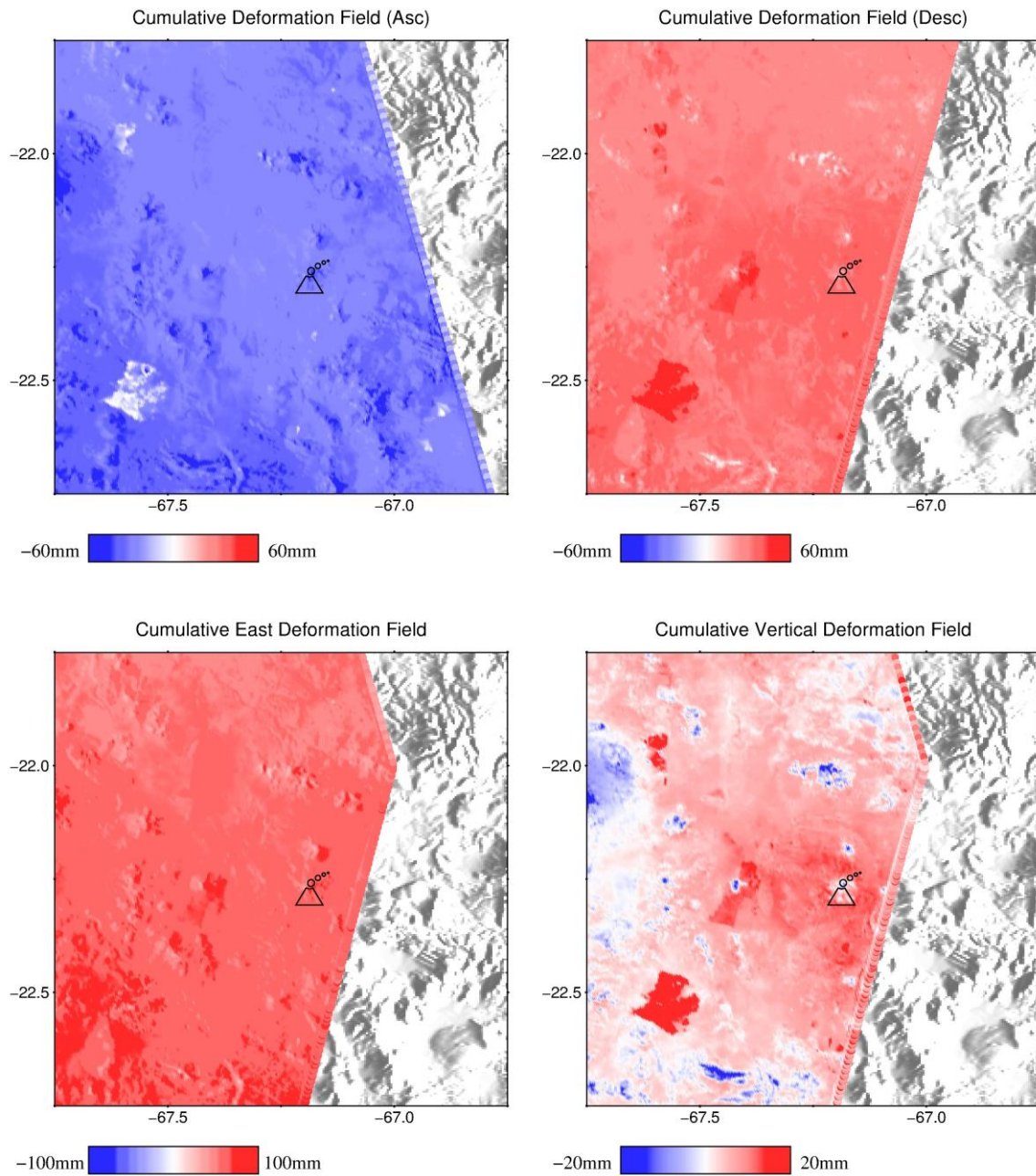


Figure S11. The decomposition of ascending and descending cumulative deformation field (Jan 2018-Oct 2021) into east and vertical deformation field, near the Uturuncu volcano. The ascending and descending cumulative deformation fields are obtained by fitting the whole observation period with one linear velocity.

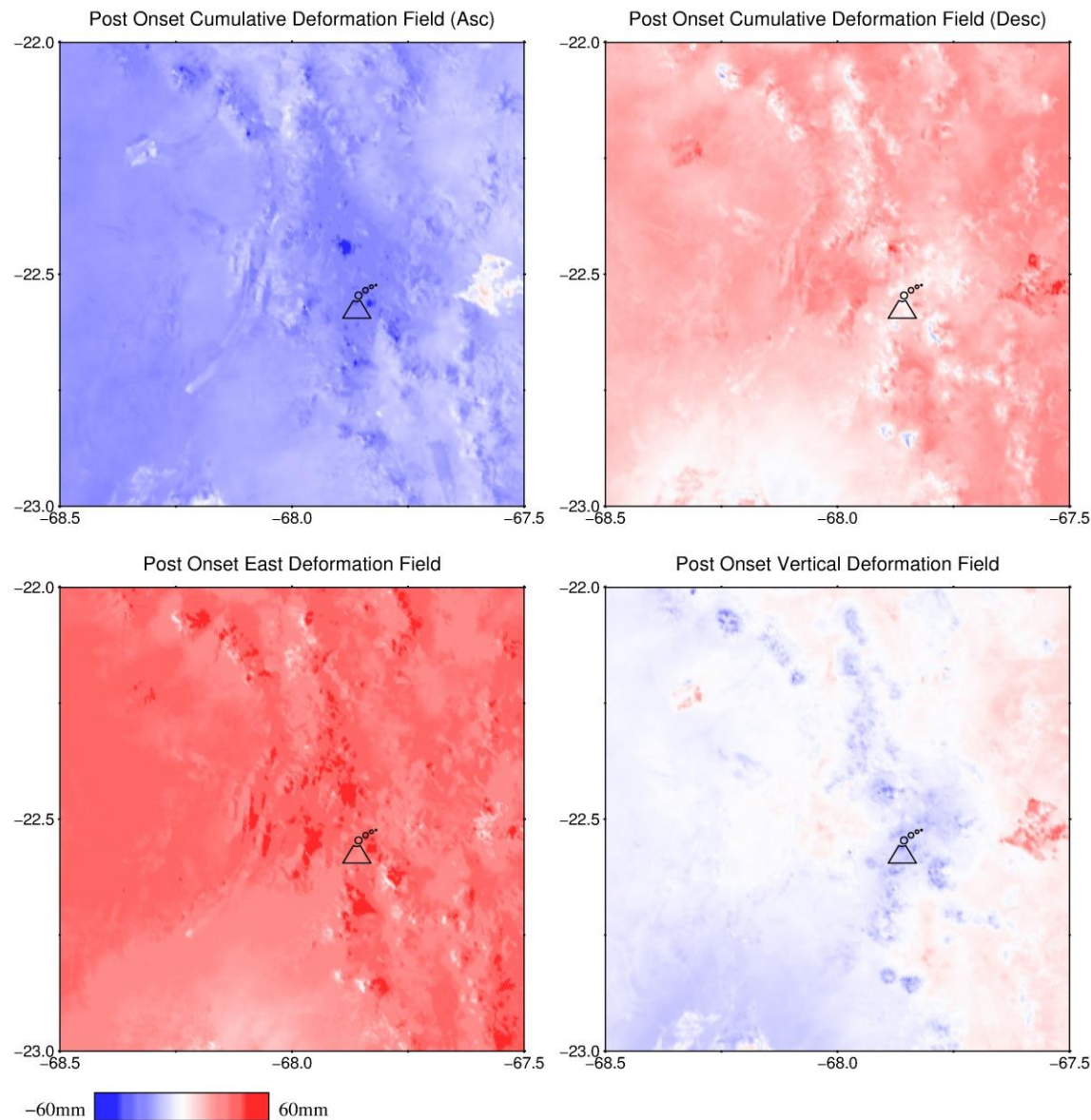


Figure S12. The decomposition of ascending and descending post onset time cumulative deformation field (Dec 2019-Oct 2021) into east and vertical deformation field, near the Putana volcano. The ascending and descending cumulative deformation fields are obtained by fitting equation 1 in the main text.

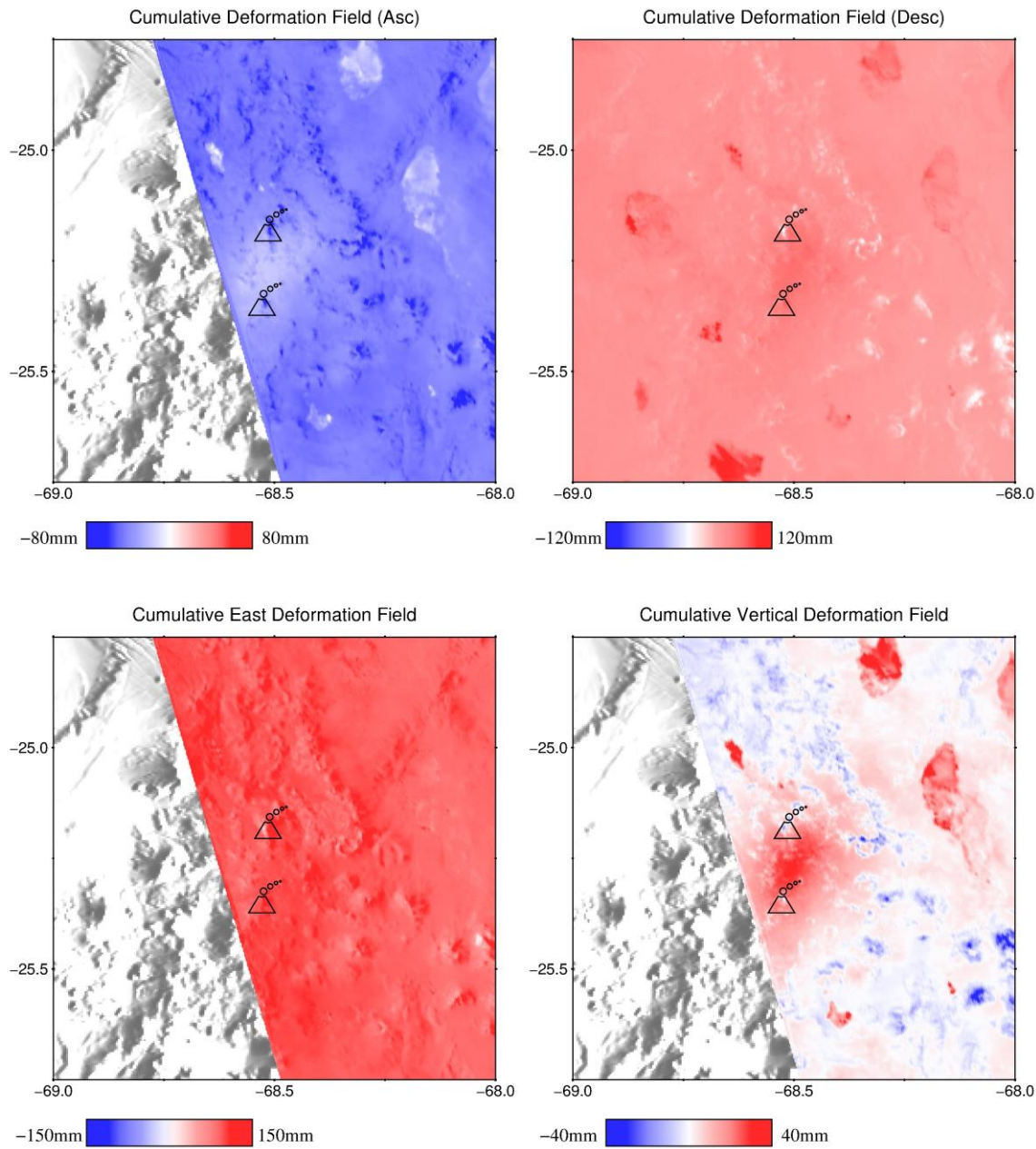


Figure S13. The decomposition of ascending and descending cumulative deformation field (Jan 2018-Oct 2021) into east and vertical deformation field, near the Lazufre (Lastarria & Azufre) volcano. The ascending and descending cumulative deformation fields are obtained by fitting the whole observation period with one linear velocity.

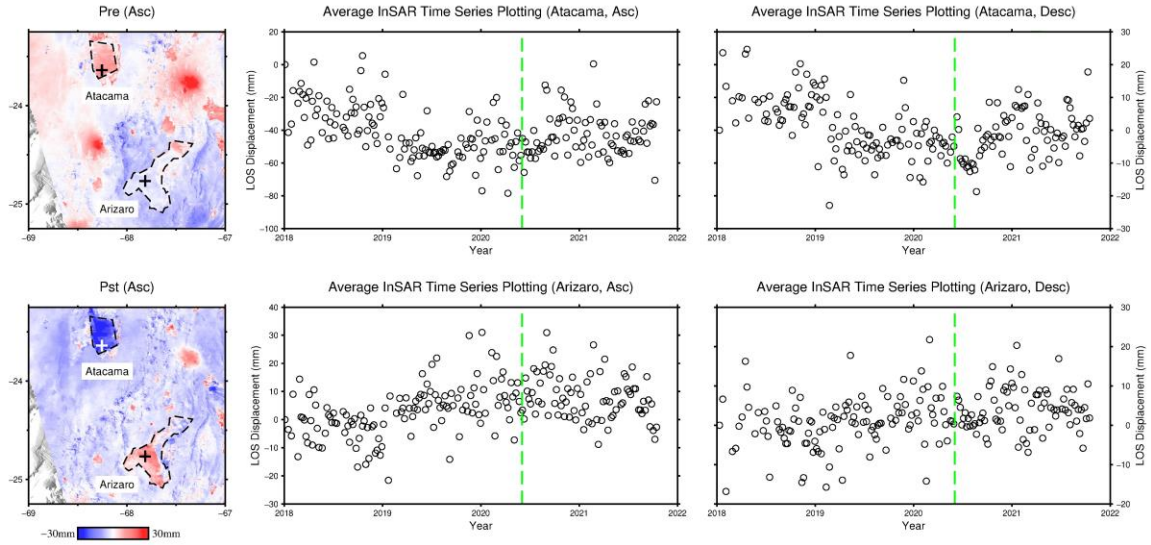


Figure S14. Average InSAR time series over Salar de Arizaro and Atacama region on ascending and descending tracks data. Black dashed polygons, plus symbols, and green dashed lines indicate the approximate boundaries of Salar regions, the location of pixels plot on the time series panels, and the event time of earthquake M_w 6.8, respectively. It shows opposite surface displacements occurrence on Salar de Arizaro and Atacama at the beginning of 2019.

	Mogi	Yang	Okada	pCDM (pECM)
X (km)	3.78	3.56	6.70	3.19
	3.30-4.19	2.94-3.85	5.99-8.05	2.71-3.65
Y (km)	5.71	6.50	11.5	5.82
	5.22-6.44	5.56-6.90	10.6-13.5	5.50-6.77
Depth (km)	9.40	9.85	12.9	5.74
	8.60-10.3	6.83-10.4	10.2-14.3	5.35-6.96
Volume Change ($\times 10^7$ m3)	1.41	1.61	2.18	1.07
	1.19-1.69	1.04-1.80	1.83-2.95	0.98-1.14

Table S1. The comparison of some main parameters from different volcanic geodetic source modelling results. The optimal values and corresponding 95% confidence intervals are provided. Here X and Y represent the location reference to the SOCM station, where positive values mean towards north or east.

Volcano Name	Monitored or Not	Fumarolic Active	Geodesy Observation	Deformation mechanism and Source Depth	Key References
Uturuncu	N	Y	InSAR from ERS, ENVISAT, Sentinel-1 (1992-2018), GPS	Magmatic. Modelled by several source types, the typical depth is 15-30 km.	Fialko & Pearse, 2012 Henderson & Pritchard, 2017 Gottsmann et al., 2017 Lau et al., 2019 Barone et al., 2019
Putana	N	Y	InSAR from ERS and ENVISAT (1992-2011)	Hydrothermal. A shallow Mogi source at 1 km depth	Henderson & Pritchard, 2013
Lascar	Y	Y	InSAR from ERS, ENVISAT, and TerraSAR-X (1992-2000, 2012-2017), GPS	Complex deformation. A combination of ongoing crater evolution processes, including gravitational slumping, cooling and compaction of eruption products, as well as possible piston-like subsidence	Pritchard & Simons, 2002 Pavez et al., 2006 Richter et al., 2017
Cerro Overo	-	-	InSAR from ERS and ENVISAT (1992-2011)	Controlled by a single reversible mechanism involving fluid accumulation and loss within the crust at ~10 km depth	Henderson & Pritchard, 2013
Lastarria & Azufre	Y	Y	InSAR from ERS, ENVISAT, RADARSAT-2, TerraSAR-X, COSMO-SkyMed, and Sentinel-1 (1995-2016), GPS	Magmatic. Modelled by several source types, the typical depth is <10 km.	Pearse & Lundgren, 2013 Henderson et al., 2017 Díaz et al., 2015

Table S2. Summary of volcanoes in our study area that have been reported to be deforming in the past few decades from previous studies. It shows whether the volcanoes have been monitored by ground observations. Here Cerro Overo presents a deformation area rather than a specific volcano and thus is not marked.